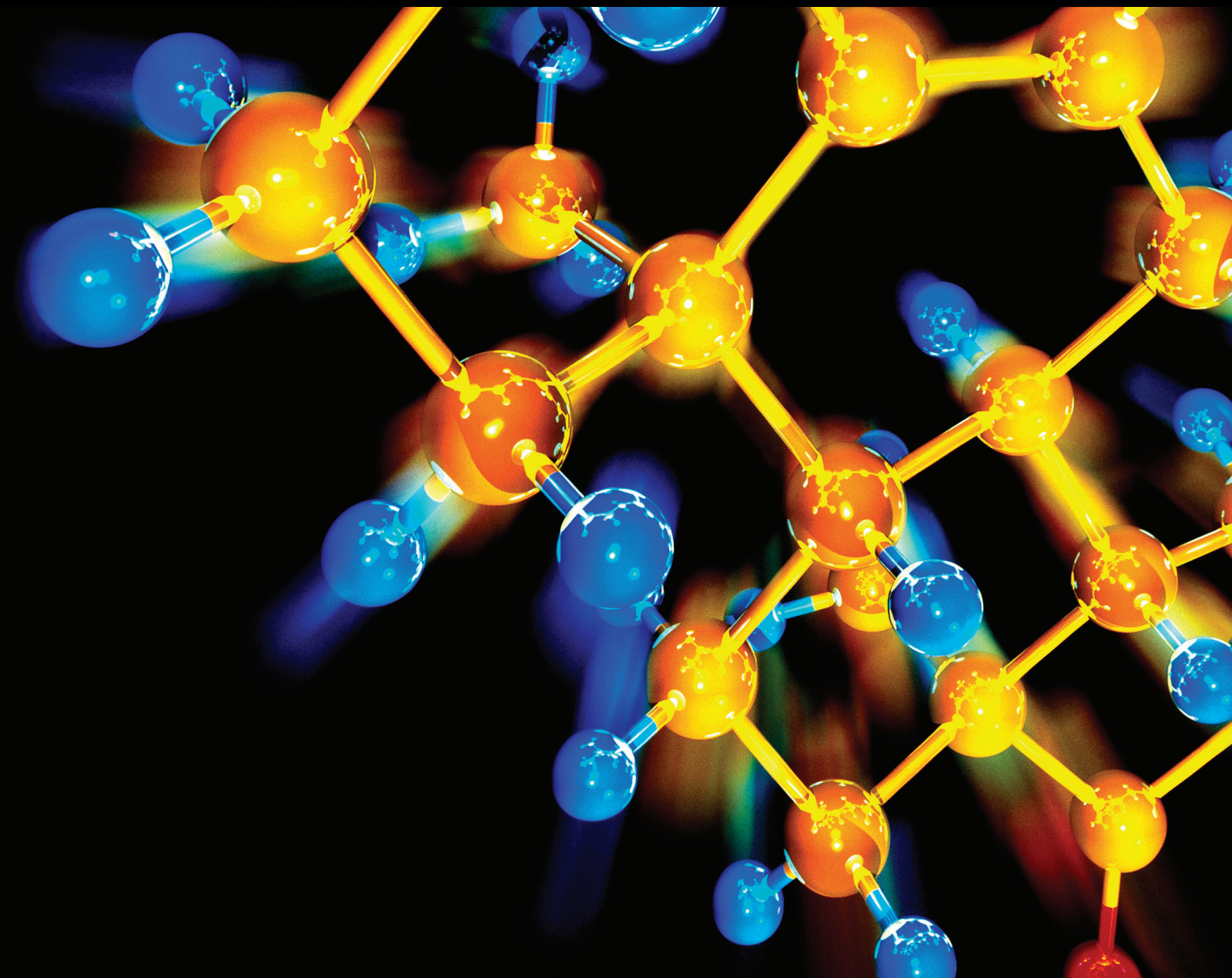


# Recent Advances in Nanomaterials for Environmental Detection and Remediation

Guest Editors: Jumin Hao, Jianfeng Zhang, Lili He, Liping Qiu, and Qichen Wang





---

# **Recent Advances in Nanomaterials for Environmental Detection and Remediation**

Journal of Chemistry

---

## **Recent Advances in Nanomaterials for Environmental Detection and Remediation**

Guest Editors: Jumin Hao, Jianfeng Zhang, Lili He,  
Liping Qiu, and Qichen Wang



---

Copyright © 2015 Hindawi Publishing Corporation. All rights reserved.

This is a special issue published in "Journal of Chemistry." All articles are open access articles distributed under the Creative Commons Attribution License, which permits unrestricted use, distribution, and reproduction in any medium, provided the original work is properly cited.

## Contents

**Recent Advances in Nanomaterials for Environmental Detection and Remediation**, Jumin Hao, Qichen Wang, Jianfeng Zhang, Lili He, and Liping Qiu  
Volume 2015, Article ID 854696, 2 pages

**Detection of Nanoscale Soil Organic Matter by Middle Infrared Spectrum for Forensic Science**, Yingzi Liu, Qiang Li, Yumei Li, Jie Bao, Zhiheng Hu, Dakui Hao, Dongxue Song, Yiwei Wang, and Min Yang  
Volume 2015, Article ID 189421, 4 pages

**Micro- to Nanoscale Morphologies and Chemical Components of Soils Investigated by SEM-EDS for Forensic Science**, Yingzi Liu, Yumei Li, Qiang Li, Jie Bao, Dakui Hao, Zhiwen Zhao, Dongxue Song, Jiajia Wang, and Zhiheng Hu  
Volume 2015, Article ID 734560, 5 pages

**Effect of Modifying Prosthetic Socket Base Materials by Adding Nanodiamonds**, Lifang Ma, Xiaogang Hu, Shizhong Zhang, and Yu Chen  
Volume 2015, Article ID 481707, 7 pages

**Design of Polymeric Nanofiber Gauze Mask to Prevent Inhaling PM2.5 Particles from Haze Pollution**, Xingzhou Li and Yan Gong  
Volume 2015, Article ID 460392, 5 pages

**Effects of Nanoscale Carbon Black Modified by HNO<sub>3</sub>/H<sub>2</sub>O<sub>2</sub> on Immobilization and Phytoavailability of Ni in Contaminated Soil**, Jiemin Cheng, Lei Yu, Tong Li, Yuzhen Liu, Chengxiu Lu, Tingting Li, and Hanwei Wang  
Volume 2015, Article ID 839069, 7 pages

## Editorial

# Recent Advances in Nanomaterials for Environmental Detection and Remediation

Jumin Hao,<sup>1</sup> Qichen Wang,<sup>2</sup> Jianfeng Zhang,<sup>3</sup> Lili He,<sup>4</sup> and Liping Qiu<sup>5</sup>

<sup>1</sup>Agiltron Inc., 15 Presidential Way, Woburn, MA 01801, USA

<sup>2</sup>Micro Stamping Corporation, Somerset, NJ 08873, USA

<sup>3</sup>School of Environmental and Municipal Engineering, Xi'an University of Architecture and Technology, Xi'an, Shanxi 710055, China

<sup>4</sup>Department of Food Science, University of Massachusetts Amherst, Amherst, MA 01003, USA

<sup>5</sup>School of Civil Engineering and Architecture, University of Jinan, Jinan, Shandong 250022, China

Correspondence should be addressed to Jumin Hao; [jmhao0753@gmail.com](mailto:jmhao0753@gmail.com)

Received 31 May 2015; Accepted 31 May 2015

Copyright © 2015 Jumin Hao et al. This is an open access article distributed under the Creative Commons Attribution License, which permits unrestricted use, distribution, and reproduction in any medium, provided the original work is properly cited.

Environmental detection and remediation have been substantially benefiting from progress in nanomaterials and nanotechnologies in the past decades. Combining the nanomaterials and analytical techniques is very attractive to develop simple, sensitive, inexpensive, and miniaturized devices for field use for the detection of a variety of environmental contaminants. The nanomaterials also have great potential in advancing the treatment technologies for contaminated water, air, soil, and sediment. As experienced experts in the related areas for many years, we were invited to organize an editorial board to create a special issue to provide environmental research community with a forum to share innovative ideas and to present an up-to-date account of advancement in these fields.

Specifically, this special issue aims to study (a) preparation and application of various nanomaterials and nanostructures, made from metals and metal (hydro)oxides, carbon and fullerene derivatives, polymers, biomacromolecules, and their composites, for environmental detection and remediation; (b) identification and quantification of chemical, biological, and medical agents/toxins in various media (air, water, soils, and foods) based on nanomaterials and nanosensors; (c) sensing principles and mechanisms of nanomaterials based surface plasmon resonance (SPR), surface enhanced Raman scattering (SERS), fluorescence, colorimetry, and electrical and electrochemical sensing; (d) water/wastewater

treatment, air quality control, soil and sediment remediation using nanomaterials, nanocatalysts, and nanomaterials-doped membrane technology; (e) adsorption, degradation, and removal mechanisms of the environmental contaminants over nanoadsorbents and nanocatalysts and nanotechnology-based membrane separation, filtration processes, and photodegradation; (f) fate and transport and determination methods of engineered nanomaterials in environmental media; (g) demonstration and test of portable/handheld devices or prototypes for field use for pollutants detection and environmental remediation. The special issue consists of five research papers selected from many submissions. While they may not fully cover the topics mentioned above, these five papers represent the rich and many-faceted knowledge.

A paper entitled "Detection of Nanoscale Soil Organic Matter by Middle Infrared Spectrum for Forensic Science" by Y. Liu et al. evidenced that soil can provide significant assistance to forensic science by determining nanoscale soil organic matters (NSOMs) with middle infrared spectrum. In the study, eighteen soils sampled from different locations were investigated and results showed that the constituents and contents of NSOMs in the samples were dramatically different, and a NSOM fingerprint for each sample was drawn based on these characteristics. This suggests that a national or global NSOM fingerprint database could be rapidly established by the one-step middle infrared spectrum analysis for

different soil samples, which will be helpful in determining crime scenes by comparing the middle infrared spectrum of forensic soil with the NSOMs fingerprint database.

In another paper entitled "Micro- to Nanoscale Morphologies and Chemical Components of Soils Investigated by SEM-EDS for Forensic Science," Y. Liu et al. further demonstrated that Scanning Electron Microscope-Energy Dispersive Spectrometer (SEM-EDS) is a useful tool to evaluate homogeneities and diameters of the soils at nanoscale. The mass fraction and molar percentages of nine inorganic elements in all samples were analyzed by EDS. Oxygen and silicon showed the highest content in all of these samples. However, different samples exhibited their own characteristic elements, which can help in discriminating them from other samples. In this regard, SEM-EDS-based homogeneity and element analysis might be used as a fast and reliable technique for the soil criminological analysis.

A contribution to this special issue, entitled "Effects of Nanoscale Carbon Black Modified by  $\text{HNO}_3$  on Immobilization and Phytoavailability of Ni in Contaminated Soil" by J. Cheng et al., reported a surface-modified nanoscale carbon black (MCB) as Ni adsorbent in contaminated soil prepared by oxidizing the carbon black with 65%  $\text{HNO}_3$ . The surface properties of the adsorbent were characterized with zeta potential analysis, scanning electron microscopy (SEM), and Fourier transform infrared spectroscopy (FTIR). The authors investigated adsorption performance of  $\text{Ni}^{2+}$  by MCB and examined the effects of MCB on the DTPA-extractable  $\text{Ni}^{2+}$  in soil,  $\text{Ni}^{2+}$  uptake of ryegrass shoot, and growth of ryegrass. Results indicated that MCB possessed enhanced sorption capacity for Ni compared to CB and could be applied in the in situ immobilization, remediation of heavy metal contaminated saline-alkali soils, and phytoavailability.

Recently, PM2.5 (particulate matter with diameter of 2.5 microns or less) has become a major health hazard from the polluted air in many cities in China. The study by X. Li and Y. Gong in the paper entitled "Design of Polymeric Nanofiber Gauze Mask to Prevent Inhaling PM2.5 Particles from Haze Pollution" reported a polysulfone nanofiber as mask filtration material by electrospinning technique. The nanofiber mask material was characterized by SEM, air permeability test, and PM2.5 trapping experiment. The results indicate that nanofiber mask material can efficiently filter out the PM2.5 particles and simultaneously preserve a good breathability. In this regard, the nanofiber based material would be made into the comfortable and effective mask for preventing inhaling the harmful particles in haze air pollution. The nanofiber masks could be developed to commercial available masks in the future.

Finally, the contribution entitled "Effect of Modifying Prosthetic Socket Base Materials by Adding Nanodiamonds" by L. Ma et al. demonstrated that adding a predetermined amount of nanodiamonds (between 0.1 and 1.0 wt.%) to the prosthetic socket base material can increase the glass transition temperature and improve the mechanical properties of the cured base material. More importantly, the authors' investigation indicated that the nanodiamond addition to the system could reduce the amount of unreacted volatile

monomer and decrease the adverse effects of any unreacted volatile monomer on the working environment. This provides a potential for improving the method and safety for the processing and modification of prosthetic socket base materials.

Compiling these papers, we hope to enrich our readers and researchers with respect to the most recent progresses in the field of the nanomaterials for environmental detection and remediation.

## Acknowledgments

We, the guest editors, would like to appreciate all the authors for their contributions and all reviewers for their time and valuable comments to improve the quality of these papers.

*Jumin Hao  
Qichen Wang  
Jianfeng Zhang  
Lili He  
Liping Qiu*

## Research Article

# Detection of Nanoscale Soil Organic Matter by Middle Infrared Spectrum for Forensic Science

Yingzi Liu,<sup>1</sup> Qiang Li,<sup>2</sup> Yumei Li,<sup>2,3</sup> Jie Bao,<sup>2</sup> Zhiheng Hu,<sup>2</sup> Dakui Hao,<sup>4</sup>  
Dongxue Song,<sup>2</sup> Yiwei Wang,<sup>2</sup> and Min Yang<sup>2</sup>

<sup>1</sup>Department of Criminal Science and Technology, Shandong Police College, Jinan 250014, China

<sup>2</sup>School of Biological Science and Technology, University of Jinan, Jinan 250022, China

<sup>3</sup>Xinjiang Production & Construction Corps Key Laboratory of Protection and Utilization of Biological Resources in Tarim Basin, Alar 843300, China

<sup>4</sup>School of Chemistry and Chemical Engineering, University of Jinan, Jinan 250022, China

Correspondence should be addressed to Yumei Li; [mls.liym@ujn.edu.cn](mailto:mls.liym@ujn.edu.cn)

Received 30 December 2014; Accepted 21 January 2015

Academic Editor: Jumin Hao

Copyright © 2015 Yingzi Liu et al. This is an open access article distributed under the Creative Commons Attribution License, which permits unrestricted use, distribution, and reproduction in any medium, provided the original work is properly cited.

Soil is useful as a kind of trace evidence for forensic science. Thus it is very crucial to identify sources of soil. The nanoscale soil organic matter (NSOMs) can be used to differentiate soil sources because their constituents and contents are relatively stable with time but variant by location. In this study, NSOMs from eighteen regions of Shandong Province in China were examined by middle infrared spectrum ( $4000\text{--}400\text{ cm}^{-1}$ ). The results showed that the constituents and contents of NSOMs in eighteen samples were dramatically different; a NSOM fingerprint for each sample was drawn based on these characteristics. This suggests that a national or global NSOM fingerprint database could be rapidly established by the one-step middle infrared spectrum analysis for different soil samples, which will be helpful to determine crime scenes by comparing the middle infrared spectrum of forensic soil with the NSOMs fingerprint database.

## 1. Introduction

Soil as important trace evidence can provide meaningful information for criminal investigation. The constituents of soil consist of organic matter, inorganic mineral grain, chemical precipitates (such as calcium carbonate and salt crystal), dead plants, animal matter, insect carapace, bacteria, soil algae, fungi, roots of higher plants, and so forth. Forensic detection of soil evidence has been performed by comparing soil components like organic matter, heavy and light minerals, oxides, stable and radioactive isotopes, pollens, diatoms, and microorganisms, meanwhile determining physical properties, such as color, distribution of particle sizes, and density [1]. Of these characteristics, the nanoscale soil organic matter (NSOMs) are the most easily affected by environmental factors, for instance, wreathing, microorganisms present in the soil, plants in nearby soil, animal residues, and artifacts of

human beings [2]. This means soil from different places was discrepant. However, NSOMs are relatively stable in a period, which may give actual information from crime scenes.

The main constituents of NSOMs were composed of lignin, lipid or fatty acid, carbohydrate, protein, cellulose, hopane, and so forth [3]. The main functional groups of these compounds can be rapidly identified and quantified by middle infrared spectrum ( $4000\text{--}400\text{ cm}^{-1}$ ), which has become a powerful rapid assessment tool for determining soil properties [4]. In this study, eighteen soil samples from different regions in Shandong Province in China were selected and applied to Fourier transform infrared spectroscopy. Their NSOMs constituents (the main functional groups) and contents were rapidly and accurately determined. The results showed that there was a one-to-one relationship between the constituents and contents of NSOMs and the soil sources. Thus, a NSOM fingerprint was easily drawn, which suggests

that it is possible to perform the rapid batch detections for a large number of soil samples to establish a national or global NSOM fingerprint database for forensic science.

## 2. Materials and Methods

**2.1. Sample Collection.** Eighteen soil samples were collected from different regions in Shandong Province in China. Samples were named as S1 to S18, representing Heze, Qufu, Zibo, Zhuangjia (Yantai), Penglai (Yantai), Zouping County (Bingzhou), Jiaxiang County (Jining), Kenli County (Dongying), Wulian County (Rizhao), Zaozhuang, Laiwu, Liaocheng, Rongcheng (Weihai), Jiaozhou (Qingdao), South Mountainous Area (Jinan), Taian, Changyi (Weifang), Xiajin (Dezhou), and Jining, respectively.

**2.2. Sample Preparation.** Soil samples were ground down into powder and dried at 120°C for 12 hours. Then 2.5 mg of the dried soil sample was mixed with 500 mg of dry potassium bromide (KBr). The mixture was pressed into a mold (8 mm in diameter and 0.05 mm in thickness) with a pressure of  $1 \times 10^8$  kg/m<sup>2</sup>.

**2.3. Infrared Spectra.** Infrared spectra were recorded in frequency ranges from 4000 to 400 cm<sup>-1</sup> by a Fourier transform infrared spectroscopy (Bruker AXS VERTEX 70, Germany). The quantitative analysis of NSOMs was performed using KBr tablet method according to JJG-1996.

## 3. Results and Discussion

**3.1. The Organic Spectra Peak Assignment.** According to the previous investigation about the infrared spectra of soil organic matter (SOMs) [4–7], the peak assignments from S1 to S18 were analyzed. As shown in Figure 1, the peak assignment was varied with the soil source. The wide absorption peaks at 3591–3626 cm<sup>-1</sup> were the characteristics of hydroxyl groups (–OH). The small peaks at 3107–3448 cm<sup>-1</sup> and 2322–2360 cm<sup>-1</sup> were the characteristics of –NH and NH<sup>+</sup>, respectively. The peaks at 1612–1616 cm<sup>-1</sup> belonged to C=C stretching. The peaks at 1429–1635 cm<sup>-1</sup> were attributed to O–N=O/C=C stretching. The peaks at 1379–1436 cm<sup>-1</sup> were assigned to C–N=O/C=O stretching. The broad and intense stretching peaks at 1379–1384 cm<sup>-1</sup> belonged to C–H stretching. The peaks at 1006–1122 cm<sup>-1</sup> were assigned to C–O stretching. The peaks at 1000–1100 cm<sup>-1</sup> and 1014–1024 cm<sup>-1</sup> belonged to the characteristics of P–O=R and C–O–C/C–O, respectively. The peaks at 740–779 cm<sup>-1</sup> were associated with C–O–C or C–H stretching vibrations. The strong stretching peaks at 484–532 cm<sup>-1</sup> and 469–457 cm<sup>-1</sup> were attributed to P–Cl and C–X (halogen) stretching, respectively.

**3.2. Quantitative Analysis.** The numbers and types of the main functional groups in NSOMs of S1–S18 were analyzed according to the infrared data. As shown in Figure 2, the number, type, and absorbance value of the main functional groups in NSOMs varied with the source of the soil sample

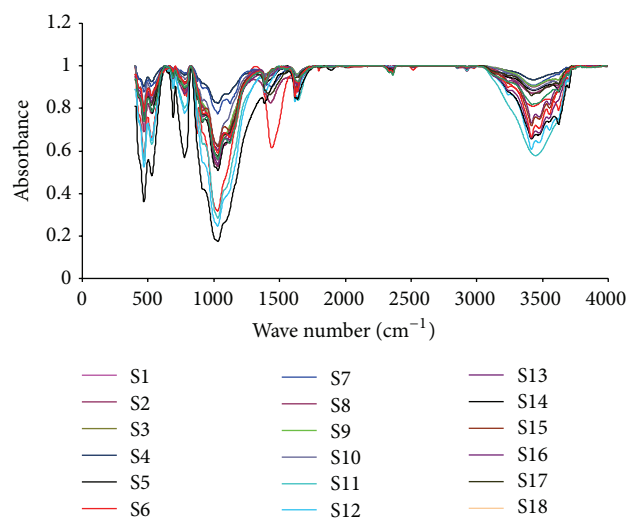


FIGURE 1: Infrared spectra of eighteen soil samples (S1 to S18).

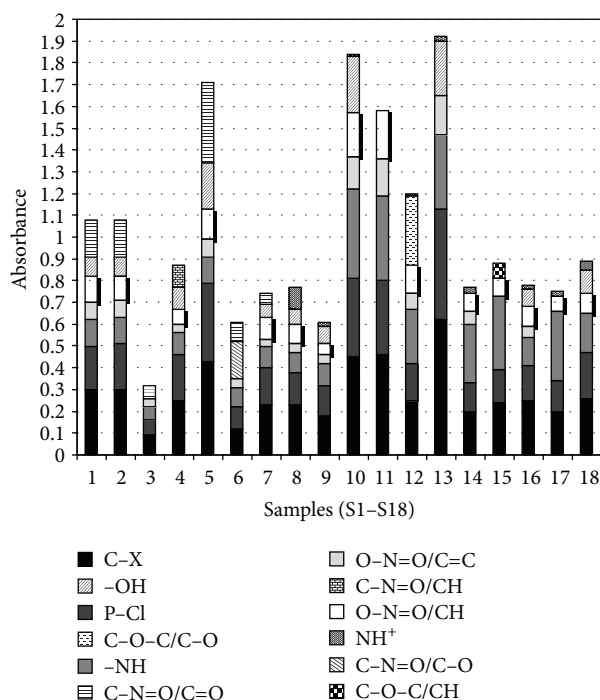


FIGURE 2: The number, type, and absorbance value of the main functional groups in NSOMs.

due to a variety of geological environments in different regions. The samples S1, S2, S4, S5, S7, S8, S9, S10, and S12 were composed of seven functional groups. S6, S13, and S18 consisted of six functional groups. S3, S11, S14, S15, and S17 contained five functional groups.

The hydroxyl group (–OH) was present in all of 18 samples, but it was infinitesimal in S6, S15, S16, and S17. There were eleven types of functional groups in S18, which indicated that this sample contained abundant organic matter [8]. By contrast, S11 and S15 only contained seven types of functional

TABLE 1: The database table design of S1 sample.

Number of functional groups	Type of functional groups	Absorbance value of functional groups			
7	C-X	0.31			
	P-Cl		0.19		
	-NH			0.13	
	O-N=O/C=C				0.09
	O-N=O/CH				0.12
	C-N=O/C-O				0.08
	-OH				0.17

groups, which suggested that the organic matter were poor in these soil samples. The relative contents of C-X and P-Cl groups in S13 were highest in all of the samples, which were probably associated with the situated chemical plants in the sampling locations [9]. However, there were scarcely any C-X and P-Cl groups in S3, which meant that the soil of the sampling location was hardly contaminated [10].

The types of the main functional groups were only halfway similar for each sample. The absorbance value of the same functional group was different as well. These differences will be a favorable reference for the analysis of the soil source using a computer program.

**3.3. NSOM Fingerprint Database.** The SOM fingerprint database of tested soil samples (S1-S18) could be established according to the difference of the main functional groups in SOMs identified by the middle infrared spectra. The scheme of SOM fingerprint database was designed as follows: the database was created and named as A. Then a table, namely B, was created in this directory, which contained some fields including number, type, and absorbance value of the main functional groups of NSOMs in each soil sample. Taking the table of S1 sample as an example, the procedure of the database table design was described (Table 1). Thus, the source of unknown soil sample may be rapidly identified using computer program through an SQL main organic functional groups query (SELECT \* FROM TABLE B WHERE B.NumberOfKind = sample's number of kind AND B.Absorbance valueOftype1 = sample's content of type1 AND . . .). This suggests that the establishment of the forensic SOM fingerprint database was feasible based on the infrared spectra analysis of SOMs, and the crime scenes will be rapidly locked using the forensic SOM fingerprint database.

## 4. Conclusions

In this study, Fourier transform middle infrared spectroscopy was applied to analyze eighteen soil samples from different regions of Shandong Province in China. The resulting infrared spectra showed that the constituents and contents of nanoscale soil organic matter (NSOMs) were varied with their sources. The main NSOM constituents of tested samples were composed of -OH, -NH, NH<sup>+</sup>, C=C, O-N=O/C=O, C-N=O/C=O, C-H, C-O, P-O=R, C-O-C, O-N=O/CH, P-Cl, and C-X with different contents. Based on these characteristics, the NSOM fingerprints of tested soil samples were

established, which could be useful for the rapid analysis of crime scenes by comparing the forensic soil with the NSOM fingerprint database.

## Conflict of Interests

The authors declare that there is no conflict of interests regarding the publication of this paper.

## Authors' Contribution

Yingzi Liu and Qiang Li contributed equally to this work.

## Acknowledgments

This work was supported by the National Natural Science Foundation of China (Projects nos. 31300045 and 31100088), Foundation of University of Jinan (XKY1324), Open Fund of Xinjiang Production & Construction Corps Key Laboratory of Protection and Utilization of Biological Resources in Tarim Basin and (BYBR1405), Shandong Province Science and Technology Development Plan (Grants nos. 2013GSF12006 and 2012GGB01172).

## References

- [1] P. Kenneth, *Geological and Soil Evidence: Forensic Applications*, CRC Press, 2007.
- [2] L. A. Dawson and S. Hillier, "Measurement of soil characteristics for forensic applications," *Surface and Interface Analysis*, vol. 42, no. 5, pp. 363-377, 2010.
- [3] R. J. Cox, H. L. Peterson, J. Young, C. Cusik, and E. O. Espinoza, "The forensic analysis of soil organic by FTIR," *Forensic Science International*, vol. 108, no. 2, pp. 107-116, 2000.
- [4] N. C. Thanasoulas, E. T. Piliouris, M.-S. E. Kotti, and N. P. Evmiridis, "Application of multivariate chemometrics in forensic soil discrimination based on the UV-Vis spectrum of the acid fraction of humus," *Forensic Science International*, vol. 130, no. 2-3, pp. 73-82, 2002.
- [5] C. Lee, T. M. Sung, H. S. Kim, and C. H. Jeo, "Classification of forensic soil evidences by application of THM-PyGC/MS and multivariate analysis," *Journal of Analytical and Applied Pyrolysis*, vol. 96, pp. 33-42, 2012.
- [6] P. Smith, "Carbon sequestration in croplands: the potential in Europe and the global context," *European Journal of Agronomy*, vol. 20, pp. 229-236, 2004.

- [7] V. F. Melo, L. C. Barbar, P. G. Zamora, C. E. Schaefer, and G. A. Cordeiro, "Chemical, physical and mineralogical characterization of soils from the Curitiba Metropolitan Region for forensic purpose," *Forensic Science International*, vol. 179, pp. 123–134, 2008.
- [8] T. Pan, M. Li, and J. Chen, "Selection method of quasi-continuous wavelength combination with applications to the near-infrared spectroscopic analysis of soil organic matter," *Applied Spectroscopy*, vol. 68, no. 3, pp. 263–271, 2014.
- [9] R. N. Okparanma and A. M. Mouazen, "Visible and near-infrared spectroscopy analysis of a polycyclic aromatic hydrocarbon in soils," *The Scientific World Journal*, vol. 2013, Article ID 160360, 9 pages, 2013.
- [10] J. Wetterlind, B. Stenberg, and R. A. V. Rossel, "Soil analysis using visible and near infrared spectroscopy," *Methods in Molecular Biology*, vol. 953, pp. 95–107, 2013.

## Research Article

# Micro- to Nanoscale Morphologies and Chemical Components of Soils Investigated by SEM-EDS for Forensic Science

Yingzi Liu,<sup>1</sup> Yumei Li,<sup>2</sup> Qiang Li,<sup>2</sup> Jie Bao,<sup>2</sup> Dakui Hao,<sup>2</sup> Zhiwen Zhao,<sup>1</sup> Dongxue Song,<sup>2</sup> Jiajia Wang,<sup>2</sup> and Zhiheng Hu<sup>2</sup>

<sup>1</sup>Department of Criminal Science and Technology, Shandong Police College, Jinan 250014, China

<sup>2</sup>School of Biological Science and Technology, University of Jinan, Jinan 250022, China

Correspondence should be addressed to Qiang Li; [chm.liq@ujn.edu.cn](mailto:chm.liq@ujn.edu.cn)

Received 19 December 2014; Accepted 21 January 2015

Academic Editor: Qichen Wang

Copyright © 2015 Yingzi Liu et al. This is an open access article distributed under the Creative Commons Attribution License, which permits unrestricted use, distribution, and reproduction in any medium, provided the original work is properly cited.

As a kind of microscale physical evidence, soil can provide significant assistance to forensic science. In this study, soil samples that were collected from eighteen different regions of Shandong Province, China, were examined by scanning electron microscope-energy dispersive spectrometer (SEM-EDS). The homogeneities and diameters of the samples were evaluated by SEM which has been applied to observe objects at nanoscale. The soil from Jiexiang, a city in Eastern Shandong Province, showed the maximal particle diameter and the sample from Liaocheng, another Eastern city in Shandong Province, showed the best homogeneity. The mass fraction and molar percentages of nine inorganic elements in all samples were analyzed by EDS. Oxygen and silicon showed the highest content in all of these samples. However, different samples exhibited their own characteristic elements, which can help to discriminate them from other samples. In this regard, SEM-EDS-based homogeneity and element analysis might be used as a fast and reliable technique for the soil criminological analysis in Shandong Province.

## 1. Introduction

Soil provides the nutrients and water required by terrestrial plants growth and exchange energy. Soil is influenced by various biotic and biological factors, such as climate, early formation of texture, microbial environment, and human activities. Therefore, the soil from various regions has tremendous differences in the components of metal, minerals, and the microbial communities [1, 2].

There is a strong connection between the soil and people's lives. Soil on the body or belongings of a person could be used as trace evidence in a large amount of criminal cases. As a kind of trace evidence, soil has played an important role in forensic science [3–6].

The physical properties of soil, including pH, color, density gradient, and inorganic components, are traditionally examined as evidences. With the development of modern technology, detection techniques for using soil as evidence are simultaneously improved [2]. Scanning electron microscopy is a type of electron microscope that produces

image of a sample by scanning it with a focused beam of electrons. The electrons interact with electrons in the sample, producing various signals containing information about the sample's surface topography and composition. Energy-dispersive X-ray spectroscopy (EDS) is an analytical technique used for element analysis or chemical characterization of samples. SEM-EDS can determine the sizes, shapes, and elemental compositions of particles, which has been adopted by many researchers to identify different particles and link them to possible sources. Cengiz et al. collected soil samples from seventeen different regions of Istanbul city, and concluded that the SEM-EDS method can discriminate the soil evidences [7]. To the best of our knowledge, morphology characteristics and elemental composition analysis about the soil particles in Shandong Province, China, have never been reported.

A biological method, T-RFLP analysis of Shandong's soil microbial community, was previously reported for forensic science [8]. As a supplement to the T-RFLP analysis, the SEM-EDS analysis technique was used as an abiotic method to

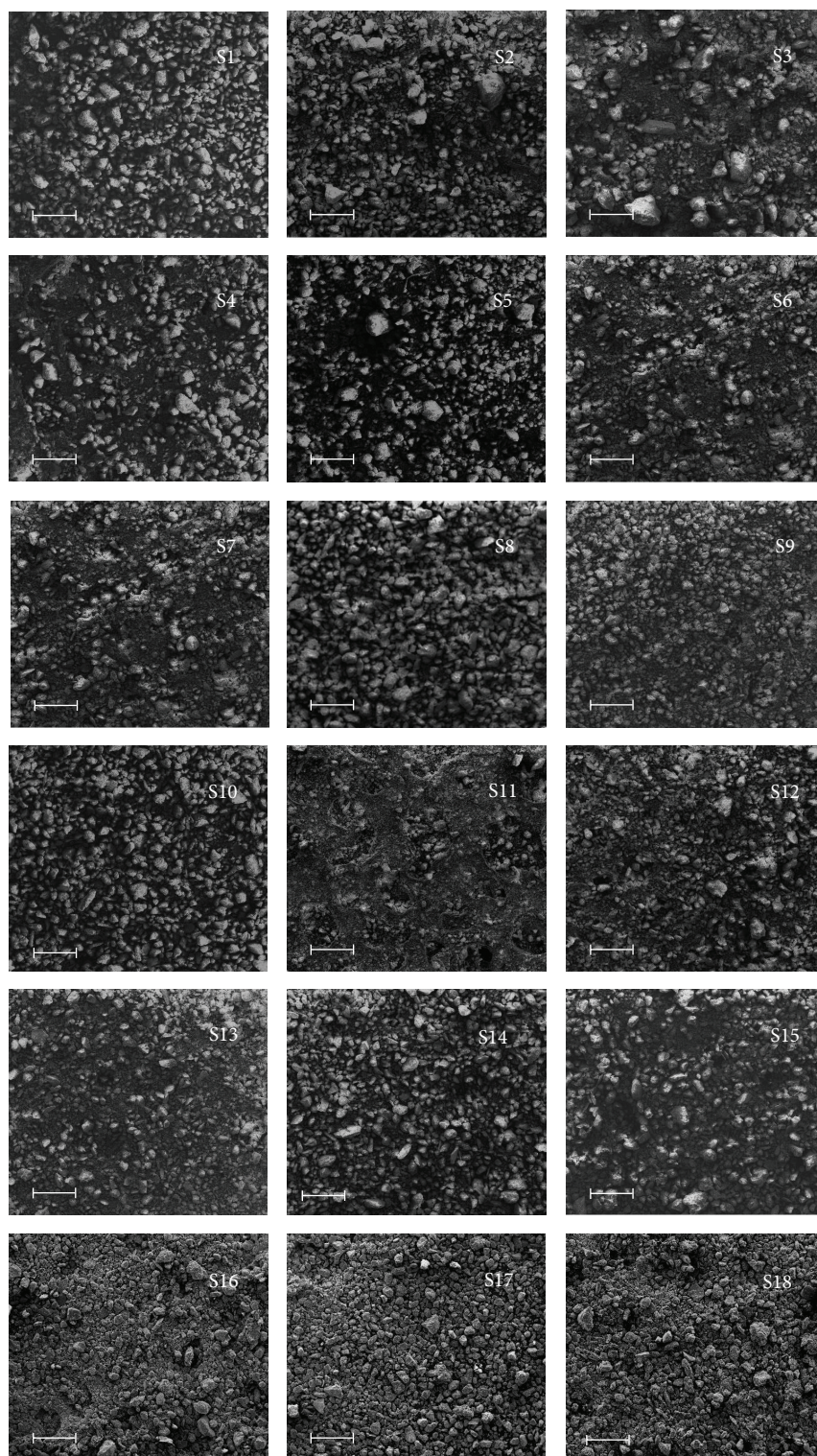


FIGURE 1: SEM images of soil from eighteen regions in Shandong province. S1 to S18, represent Zaozhuang, Yantai, Penglai (Yantai), Wulian (Rizhao), Changyi (Weifang), Rongcheng (Weihai), South mountainous area (Jinan), Liaocheng, Laiwu, Jiaozhou (Qingdao), Jiaxiang (Jining), Heze, Kenli (Dongying), Xiajin (Dezhou), Zouping (Binzhou), Qufu, Taian, and Zibo, respectively. The scale bar is 200  $\mu\text{m}$ .

analyze the morphology characteristics and elemental composition of soil samples, which were collected from eighteen regions in Shandong province, China. All samples exhibited their characteristic element contents, suggesting that it is possible to identify a specific soil sample from the sample pool by SEM-EDS analysis. This SEM-EDS-based analytical method will be helpful in the criminological analysis of trace soil samples.

## 2. Materials and Methods

**2.1. Sample Collection.** Eighteen surface soil samples were collected from different regions of Shandong Province, China. The samples were numbered from Sample 1 (S1) to Sample 18 (S18), corresponding to Zaozhuang, Yantai, Penglai (Yantai), Wulian (Rizhao), Changyi (Weifang), Rongcheng (Weihai), South mountainous area (Jinan), Liaocheng, Laiwu, Jiaozhou (Qingdao), Jiaxiang (Jining), Heze, Kenli (Dongying), Xiajin (Dezhou), Zouping (Bingzhou), Qufu, Taian, and Zibo, respectively.

**2.2. SEM-EDS Analysis.** All of the soil samples were dried for 72 hours in an oven at 110–120°C in order to remove moisture. Before they were subjected to the SEM-EDS analysis, samples were coated with a layer of gold using a gold-plated machine for 120 s. Sample analysis was performed in a Hitachi S-2500 Scanning Electron Microscope. The images were quantitatively analyzed with the software Image J [9]. SEM was equipped with an Oxford 3294X energy dispersive spectroscopic detector and was automated by Oxford Instruments INCA Energy and Feature Software. The results were detected and recorded with the Genesis 60E software.

### 2.3. Results and Discussions

**2.3.1. SEM-EDS Analysis of the Samples.** SEM is capable of imaging at a much higher resolution than light microscopes, owing to the small de Broglie wavelength of electrons. This property enables samples to be examined in fine details, as small as a single column of atoms, which is tens of thousands of times smaller than the smallest resolvable object under a light microscope. Objects can be observed in the limit of 0.1 nm ( $10^{-10}$  m). SEM images of the eighteen soil samples from different regions of Shandong Province were shown in Figure 1. All the soils are composed of micrometer-scale grains which consist of smaller particles with nanoscale structure characterization. The particle sizes of S1, S8, S10, and S13 were more homogeneous than those of others. Due to the presence of larger particles, S2, S5, and S6 were inhomogeneous, while S8 was the most homogeneous in all of the tested samples.

The particle area of these soil samples is shown in Figure 2. Samples from different regions showed varied diameters. For all of the samples, the area of soil particles was generally in the range of 100 to 500  $\mu\text{m}^2$ . The increasing order of particle sizes was S11, S7, S18, S13, S12, S9, S16, S17, S15, S14, S4, S3, S2, S10, S1, S5, S6, and S8.

There are various elements in soil, such as oxygen, silicon, aluminum, iron, calcium, sodium, potassium, magnesium,

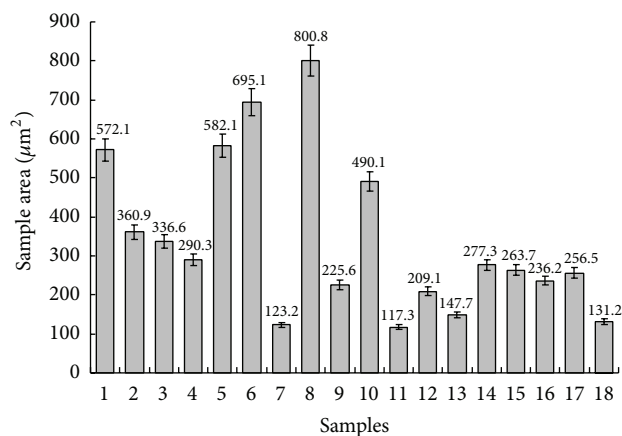


FIGURE 2: The particle area of soil samples from eighteen regions in Shandong province. Each bar represented the mean  $\pm$  SD of three replicates.

and titanium. Soil samples from different environments contained varied elements, which were characterized by element types and their content ratios.

The mass fraction and the atomic percentage of nine elements from the eighteen samples were measured by EDS. As shown in Figure 3, the contents of oxygen and silicon were the highest in all of the samples, because they are the composition elements of  $\text{SiO}_2$  and silicate, two of the most important components of soil. The contents of sodium and aluminium were relatively stable in all of these samples and ranged from 6.53% to 10.61% and from 0.46% to 1.54%, respectively. Contents of other elements varied obviously among different samples. Contents of calcium and magnesium in S11, S12, and S13 were higher than other samples, because many lands in Kenli, Xiajin, and Zouping are saline and alkaline. The content of the element titanium was the highest in S3 in comparison with all of the other samples, and the contents of the elements iron and potassium in S3 were the lowest, because this sample was collected near a coating plant. S9, S12, and S18 contained the lowest amount of magnesium, 0.98%, 0.80%, and 0.87%, respectively. The contents of the element calcium in the soil samples S1, S6, and S7 were higher than those in other samples, likely due to the native limestone constituents.

The atomic percentages of oxygen, silicon, sodium, and aluminium were relatively stable in all of these samples. Contents of calcium and magnesium were higher in S11, S12, and S13 than other samples. The atomic percentage of nine elements (Figure 4) showed the same trend as the mass fraction in Figure 3.

## 3. Conclusion

SEM-EDS-based analytical method could be used for the automatic examination and measurement of the geometric and morphological parameters, including the homogeneities and particle sizes of soil samples, which are important for the identification of the soil. The difference in soil elemental

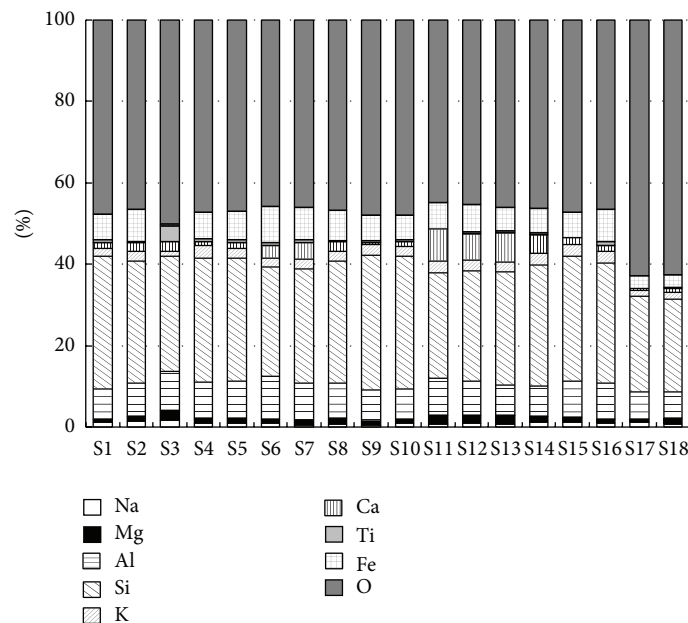


FIGURE 3: Element mass fraction of soil samples from eighteen regions in Shandong province.

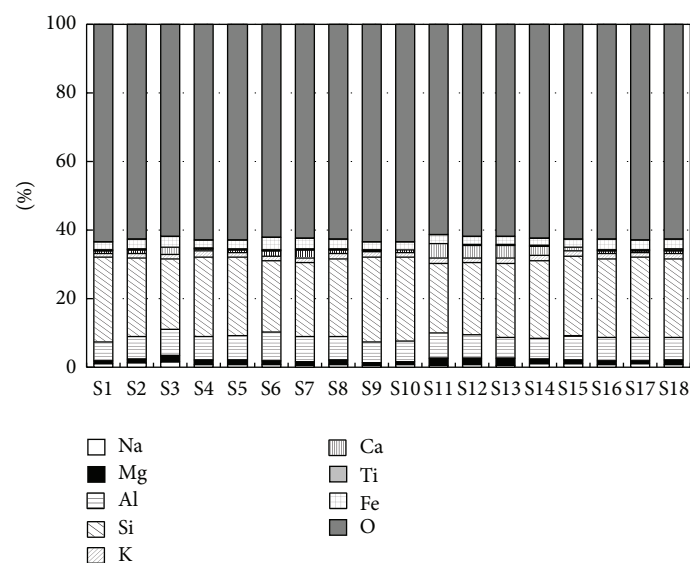


FIGURE 4: Element atomic percentage of soil from eighteen regions in Shandong Province.

components represents the variety of the soil texture from different regions, which is important when narrowing the tracking range of investigation. As a soil database in China is still in its infancy, this research will be helpful in performing the convenient batch detections of a large number of soil samples to establish a national and global SEM-EDS database for forensic science.

### Conflict of Interests

The authors declare that there is no conflict of interests regarding the publication of this paper.

### Authors' Contribution

Yingzi Liu and Yumei Li contributed equally to this work.

### Acknowledgments

This work was supported by the National Natural Science Foundation of China (Project nos. 31100088 and 31300045), Shandong province science and technology development plan (Grant nos. 2013GSF12006 and 2012GGB01172), Foundation of University of Jinan (XKY1324), and Xinjiang Production & Construction Corps Key Laboratory of Protection

and Utilization of Biological Resources in Tarim Basin (Grant no. BRYB1405).

## References

- [1] Y. Ge, L. Hu, and S. Chen, "Application and examination methods of soil for forensic science," *Journal of Chinese Legal Medical Science*, vol. 19, no. 4, pp. 260–261, 2004.
- [2] S. A. Larson, *Developing a High Throughput Protocol for Using Soil Molecular Biology as Trace Evidence*, University of Nebraska-Lincoln, Lincoln, Neb, USA, 2012.
- [3] B. D. Lee, T. N. Williamson, and R. C. Graham, "Identification of stolen rare palm trees by soil morphological and mineralogical properties," *Journal of Forensic Sciences*, vol. 47, no. 1, pp. 190–194, 2002.
- [4] M. Horrocks and K. J. Walsh, "Pollen on grass clippings: putting the suspect at the scene of the crime," *Journal of Forensic Sciences*, vol. 46, no. 4, pp. 947–949, 2001.
- [5] L. A. Daugherty, "Soil science contribution to an airplane crash investigation, Ruidoso, New Mexico," *Journal of Forensic Sciences*, vol. 42, no. 3, pp. 401–405, 1997.
- [6] N. Petraco and T. Kubic, "A density gradient technique for use in forensic soil analysis," *Journal of Forensic Sciences*, vol. 45, no. 4, pp. 872–873, 2000.
- [7] S. Cengiz, A. C. Karaca, I. Çakir, H. B. Üner, and A. Sevindik, "SEM-EDS analysis and discrimination of forensic soil," *Forensic Science International*, vol. 141, no. 1, pp. 33–37, 2004.
- [8] J. Wang, Y. Li, Z. Zhao et al., "T-RFLP analysis of soil microbial community from shandong province for forensic science," *Advanced Materials Research*, vol. 599, pp. 250–253, 2012.
- [9] <http://rsb.info.nih.gov/>.

## Research Article

# Effect of Modifying Prosthetic Socket Base Materials by Adding Nanodiamonds

Lifang Ma,<sup>1,2</sup> Xiaogang Hu,<sup>3</sup> Shizhong Zhang,<sup>1</sup> and Yu Chen<sup>1</sup>

<sup>1</sup>Beijing Institute of Technology, Beijing 100081, China

<sup>2</sup>National Research Center for Rehabilitation Technical Aids, Beijing 100176, China

<sup>3</sup>Beijing Grish Hitech Co., Ltd., Beijing 100085, China

Correspondence should be addressed to Lifang Ma; malifang@sohu.com

Received 23 September 2014; Accepted 19 November 2014

Academic Editor: Jumin Hao

Copyright © 2015 Lifang Ma et al. This is an open access article distributed under the Creative Commons Attribution License, which permits unrestricted use, distribution, and reproduction in any medium, provided the original work is properly cited.

The curing process of prosthetic socket base materials requires attention owing to a series of associated problems that are yet to be addressed and solved. However, to date, few relevant studies have been reported. In this paper, nanodiamonds modified with a silane coupling agent were dispersed into a prosthetic socket base material, and the performance of the modified base materials was investigated. Adding a predetermined amount of nanodiamonds to the prosthetic socket base material increased the glass transition temperature, improved the mechanical properties of the cured base material, and reduced the influence of the volatile gas formed during the curing process on the environment. With increasing nanodiamond contents, the glass transition temperature increased and the mechanical properties improved slightly. Owing to the high thermal conductivity of the nanodiamonds, the localized heat, as a result of the curing process, could be dissipated and released. Thus, adding nanodiamonds led to a more uniform temperature field forming in the curing system. This improved the curing process and reduced the formation of volatile monomers, thereby decreasing the adverse impact of the generated volatile gases on the environment. All of these provide a potential strategy for modifying prosthetic socket base materials.

## 1. Introduction

A prosthesis is an artificial limb that is produced and assembled to restore the human body form and function and compensate for deficiencies caused by amputation. The installation of a prosthesis is a crucial step for the rehabilitation and reintegration of the amputee into society. The prosthetic socket is an important part that connects the patient's stump to the prosthesis and thus plays an important role in determining the performance of the prosthesis. However, to date, studies on prosthetic socket materials, particularly their preparation and characterization, are rarely reported.

The most common base materials employed for prosthetic sockets are modified poly(methyl methacrylate)-based fiber composite materials fabricated in a two-step process. The first step involves using methyl methacrylate (MMA) monomers to synthesize prepolymers and subsequently generating a modified base material for prosthetic socket

fabrication. The second step involves curing the modified base material and fiber material at ambient temperature to obtain the prosthetic socket. The performance of the base material plays a very important role in the following process for obtaining a comfortable, wearable prosthetic socket.

Currently, there are some problems associated with preparing prosthetic socket base materials such as instability of the curing process under ambient temperature, the occurrence of localized heat during the curing process, and related difficulties in heat release. Because the curing reaction of the base material is exothermic, localized heat concentration typically occurs during the curing process. Consequently, this instigates a high internal thermal stress in the base material, causing voids and cracks to form, thereby reducing the performance of the prosthetic socket material. This phenomenon is usually attributed to the poor thermal conductivity of the base material [1, 2]. During the curing process, the localized heating rate is high and heat release is

difficult, thereby generating a nonuniform temperature field in the curing system. Extremely high local temperatures can also result in increased volatility of the MMA monomer in the base material—MMA is a volatile and colorless gas with a pungent smell—causing adverse effects on the working environment during the curing reaction [3, 4].

Currently, several studies have been reported which focus on the improvement of the thermal conductivity of resin materials through the addition of nanoparticles [5, 6]. However, these studies mainly focus on the overall thermal conductivity of the prepared material and ignore the release of localized heat in the socket material during the curing process. Nanodiamonds exhibit excellent biocompatibility and mechanical and thermal conducting properties, and numerous studies have reported the preparation of nanodiamond-resin composite materials [7–16]. However, using nanodiamonds to improve the curing process of prosthetic sockets remains unexplored. In this paper, modified nanodiamonds were dispersed into the prosthetic socket base material, and the effect of the nanodiamonds on the curing process and performance of the cured base material was studied. In particular, the formation of volatile gases during the curing process and their influence on the environment were examined. The influence of volatile gases on the properties of the cured base material was also investigated.

## 2. Experimental Section

**2.1. Materials.** MMA, benzoyl peroxide (BPO), and *N,N*-dimethylaniline were obtained from Tianjin Fuchen Chemical Reagent Factory (Tianjin, China). Prior to the experiments, MMA was purified by vacuum distillation. The dicyclohexyl phthalate esters were purchased from Sinopharm Chemical Reagent Co., Ltd. (Tianjin, China), and phenyl salicylate was obtained from Beijing Hengye Zhongyuan Chemical Co. (Beijing, China). Nanodiamonds modified with a silane coupling agent were obtained from Beijing Guoruisheng Technology Co., Ltd. (Beijing, China).

### 2.2. Methods

**2.2.1. Preparation of the Base Material.** A four-neck flask was used as the polymerization reactor, which was equipped with an electric stirrer, a thermometer, a reflux condenser, and a nitrogen inlet. MMA (97.5 wt.%), BPO (0.5 wt.%), dicyclohexyl phthalate ester (0.75 wt.%), and phenyl salicylate (0.75 wt.%) were added to the flask to initiate polymerization at 70 °C in a dry nitrogen atmosphere for 20–25 minutes. Following cooling of the resulting prepolymer to room temperature, *N,N*-dimethylaniline (0.7 wt.%), saccharin (0.2 wt.%), and the inhibitor (0.1 wt.%) were added, and the base material was obtained after thoroughly mixing the material.

**2.2.2. Modification of the Base Material with Nanodiamonds.** Our previous modification experiments showed that nanodiamond particles were readily precipitated from the base material when the nanodiamond content was above 1 wt.%. Therefore, in this study, the nanodiamond content was varied between 0 and 1 wt.%. The base material was evenly mixed

with different contents of nanodiamonds (0.1, 0.2, 0.3, 0.5, 0.75, and 1 wt.%) using sonication and a defoaming machine. The resulting product was filtered with a sieve to obtain the modified base material.

**2.2.3. Curing Reaction at Room Temperature.** The curing agent was added to the base material at room temperature, simulating the actual preparation and processing conditions employed for prosthetic sockets.

### 2.3. Sample Characterization

**2.3.1. Fourier Transform Infrared Spectroscopy (FTIR).** For sample preparation, pellets were prepared by mixing the matrix material with KBr. The pellet was then characterized using a Shimadzu Iffinity-21 Fourier transform infrared spectrophotometer. The resolution was set to 4 cm<sup>-1</sup> and the scan number to 16.

**2.3.2. Differential Scanning Calorimetry.** A Shimadzu DSC-60 differential scanning calorimetry (DSC) apparatus was used to determine the glass transition temperature of the base material in the temperature range from -250 °C to -50 °C at a heating rate of 10 °C min<sup>-1</sup>. The sample mass used for analysis was between 5 and 8 mg. For the DSC experiments, nitrogen was used as a protective gas at a flow rate of 30 mL min<sup>-1</sup>.

**2.3.3. Evaluation of the Mechanical Properties of the Base Materials.** An in-house-built WDT-type universal testing machine was used to measure the flexural strength and elastic modulus of the samples. Three-point bending tests with a specimen span of 34 mm and a loading speed of 5 mm min<sup>-1</sup> were performed according to the GB/T 1449-2005 standard. A domestic HXD-TM-type microhardness tester was used to measure the microhardness of the cured material.

**2.3.4. Determination of the Curing Peak Temperature of the Reaction System.** The curing agent was mixed with 50 g of the base material and stirred to obtain a uniform mixture. The mixture, contained in a tube, was then placed in a water bath equipped with a thermometer at a set temperature. The SPI method was used as a reference for the temperature measurements. Owing to the specific technical requirements of the prosthetic socket preparation process, the temperature of the water bath was controlled at 25 °C.

**2.3.5. Determination of the Concentration of MMA in Air during the Curing Process [3, 4].** The concentration of MMA in air during the curing process was determined by gas chromatography. The volatilized MMA in the air was collected by activated carbon contained in a tube. Methanol solution was used for desorption and a 5% PEG-6000-containing column was used for separation. A hydrogen flame ionization detector was used to measure the concentration of MMA in the air during the curing process.

**2.3.6. Electron Microscopy Analysis.** Prior to analysis, the samples were quenched in liquid nitrogen for 30 min to allow

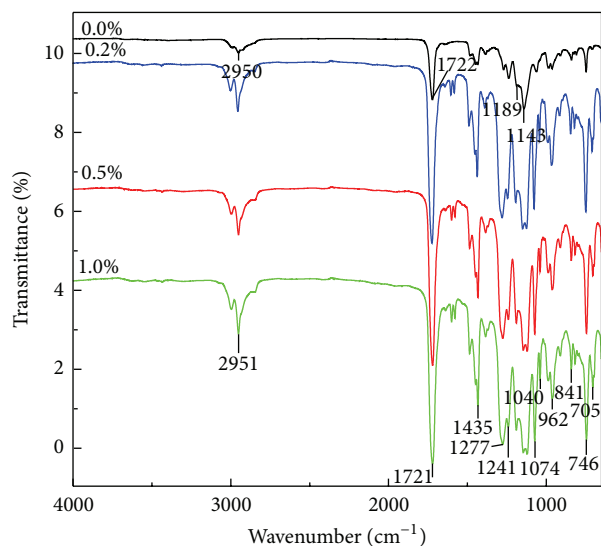


FIGURE 1: FTIR spectra of the cured base materials prepared with varying nanodiamond contents.

cracks to form. After being coated with gold, the samples were investigated by scanning electron microscopy (Hitachi S-4800) on a microscope operating at an acceleration voltage of 20 kV. Transmission electron microscopy analysis was then performed on slices of the samples on an FEI 300 kV field-emission transmission electron microscope.

### 3. Results and Discussion

**3.1. FTIR Spectra of the Cured Base Materials.** After the curing reaction of the nanodiamonds-containing base materials was completed, the base materials were characterized by FTIR spectroscopy. Figure 1 shows the FTIR spectra of the cured base materials prepared with varying nanodiamond contents. The broad absorption peak at  $2950\text{ cm}^{-1}$  was attributed to the symmetric and antisymmetric stretching vibrations of the C-H bonds in the  $-\text{CH}_3$  and  $-\text{CH}_2-$  groups. After the nanodiamonds were added, the intensity of the peak ( $2950\text{ cm}^{-1}$ ) increased and became broader because of the existing silane coupling agent in the nanodiamonds. The peaks corresponding to C-C-O-C stretching vibrations at 1143, 1189, 1241, and  $1277\text{ cm}^{-1}$  were similar to the characteristic bands of PMMA, whereas the intensity of the peaks at 1435 and  $1277\text{ cm}^{-1}$  substantially increased, confirming the deformation vibration of the Si- $\text{CH}_2$  bonds. Additionally, the intensity of the C=O stretching vibration absorption peak at  $1722\text{ cm}^{-1}$  increased with increasing nanodiamond contents.

Absorption peaks in the range  $700\text{--}900\text{ cm}^{-1}$  were attributed to the stretching vibration of the Si-C bond. The peak at  $962\text{ cm}^{-1}$  was attributed to the stretching vibration of the Si-O-C bond, and that at  $1040\text{ cm}^{-1}$  was attributed to the stretching vibration of the Si-O-Si bond. The presence of these peaks confirmed the existence of the silane coupling agent, thereby indicating that it was successfully grafted to the surface of the nanodiamonds through Si-O-C bonds [10].

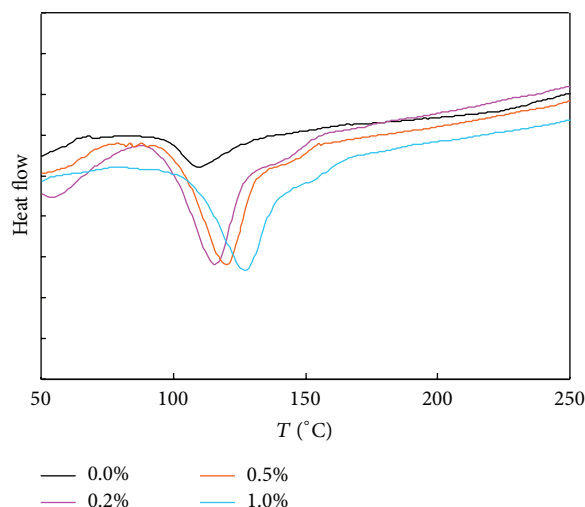


FIGURE 2: DSC curves of the base material containing varying amounts of nanodiamonds.

In summary, FTIR analysis revealed that the silane coupling agent molecules grafted to the surface of the nanodiamonds through hydrogen bonds. Additionally, self-polymerization of the silane coupling agent molecules led to the formation of Si-O-Si bonds and a layered network structure. The hydroxyl groups on the surface of the base material may indirectly combine with the nanodiamond particles via hydrogen bonding between the hydroxyl groups and the carbonyl groups of the silane coupling agent molecules [9, 10].

**3.2. Glass Transition Temperature of the Cured Base Material.** Figure 2 shows that the glass transition temperature ( $T_g$ ) of the base material gradually increased with increasing nanodiamond content. Nanodiamonds modified with the silane coupling agent could be better dispersed in the base material because of their small size. This would enhance the interaction between the macromolecules through interactions between the polar groups in the macromolecular PMMA chains of the base material and those in the silane coupling agent grafted to the nanodiamond surface. However, the added nanodiamonds occupied the void spaces between the macromolecules, thus inhibiting the movement of the macromolecular chains. These two factors led to a significant increase in the activation energy associated with the movement of the PMMA segment in the base material, resulting in increased glass transition temperatures.

**3.3. Mechanical Properties of the Cured Base Material.** Table 1 shows the mechanical properties of the base material prepared with varying amounts of nanodiamonds. The cured nanodiamond-containing base materials displayed slightly improved mechanical properties. The slight improvement was mainly due to the larger steric hindrance and stronger interactions between the modified nanodiamonds and the macromolecules in the base material. Consequently, the modified nanodiamonds were more stable in the base

TABLE 1: Mechanical properties of the cured base material prepared with varying nanodiamond contents.

Nanodiamond content (wt.%)	Compression strength	Tensile strength (MPa)	Elastic modulus (MPa)	Microhardness
0.0	73.46 ± 1.56	39.23 ± 1.69	980.75 ± 78.38	9.17
0.2	74.20 ± 1.07	39.86 ± 1.35	1017.43 ± 52.12	10.53
0.5	77.55 ± 1.90	43.47 ± 1.21	1123.87 ± 28.71	13.15
1.0	79.32 ± 1.88	44.91 ± 1.39	1198.62 ± 48.40	13.29

materials. After the curing agent was added, the interaction between the silane coupling agent molecules on the nanodiamond surface and the C=C double bonds and hydrogen bonds in the substrate molecules was activated. The activated bonds randomly attracted adjacent double bonds and hydrogen bonds to form new chemical bonds that interwove and self-polymerized to generate a three-dimensional network structure. The combination of the nanodiamond particles with the base material via chemical bonds led to enhanced mechanical properties of the cured base material. However, improvement was only marginal because of the low nanodiamond content.

**3.4. Temperature Change in the Curing Reaction of the Base Materials.** Owing to the technical requirements of the prosthetic socket preparation process, the base material should exhibit long-term stability for storage, whereas the curing reaction, once initiated, must be promptly completed under normal temperature. The curing reaction of the prosthetic socket base material mainly involves reaction of the PMMA prepolymers initiated by *N,N*-dimethylaniline and BPO. *N,N*-Dimethylaniline is a catalyst towards promoting the activity of BPO. The O–O bond in BPO decomposes to form two active groups, which react with the PMMA prepolymer, breaking the C=C double bonds and initiating further polymerization of the prepolymers. During the polymerization process, part of the *N,N*-dimethylaniline generates active nitrogen radicals that can initiate polymerization of the prepolymer. Both the high heating rate and relatively high viscosity of the prepolymers lead to the generation of localized curing heat, which is difficult to dissipate, thus creating a nonuniform temperature field in the system. In particular, bubbles resulting from the evaporation of unreacted MMA monomers will form under a local high temperature. All of these factors have a direct impact on the performance and future usability of the prosthetic socket material.

Figure 3 shows the change in the temperature in the reaction system following the addition of the curing agent to the base materials with different nanodiamond content. With increasing nanodiamond content, the peak temperature during the curing reaction of the base material gradually decreased. At a nanodiamond content of 1 wt.%, the peak temperature decreased by more than 10°C. Therefore, adding nanodiamonds is an effective means of reducing the peak temperature and increasing the uniformity of the curing system temperature field. Concurrently, the number of bubbles generated during the curing process is reduced.

**3.5. Determination of Monomer Content in Air during the Curing Reaction.** MMA is a volatile and colorless gas with a

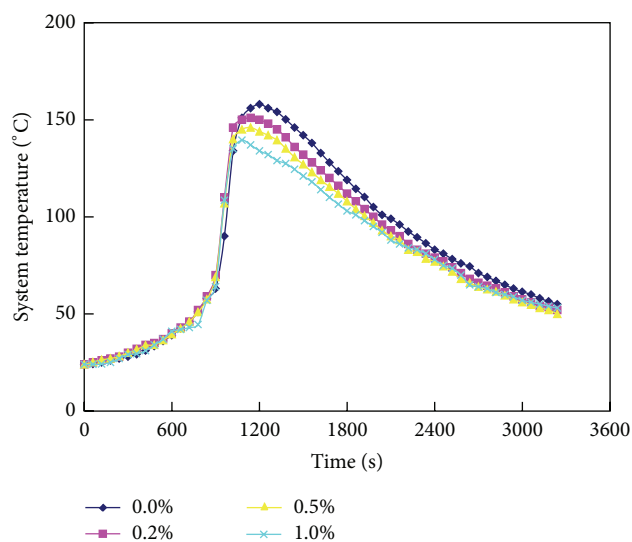


FIGURE 3: Temperature associated with the curing reaction of the base materials prepared with varying nanodiamond contents.

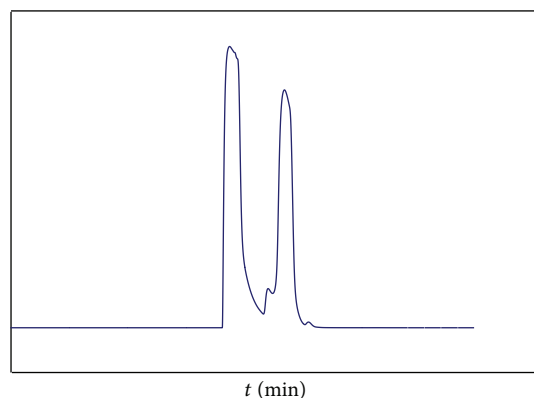


FIGURE 4: Chromatogram of methanol and methyl methacrylate.

pungent odor. Long-term exposure to poly-MMA can lead to chronic poisoning in humans, posing serious health hazards. The main health hazard is damage to the nervous system; in rare cases, exposure may cause toxic encephalopathy or teratogenesis. Additionally, MMA has some carcinogenic characteristics [3, 4]. Thus, any unreacted MMA monomers in the prosthetic socket base material are very likely to volatilize under local high temperatures, and the residual MMA monomers can result in contamination of the working environment. Table 2 lists the content of the MMA monomers in air during the curing process of the base

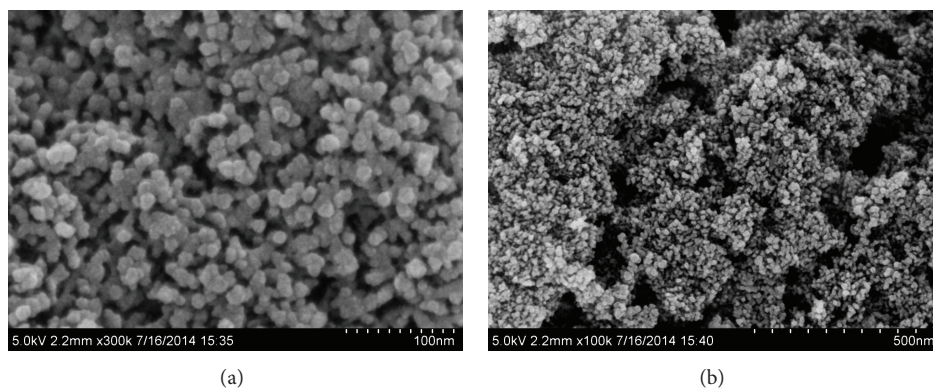


FIGURE 5: Representative scanning electron microscopy images of the modified nanodiamonds.

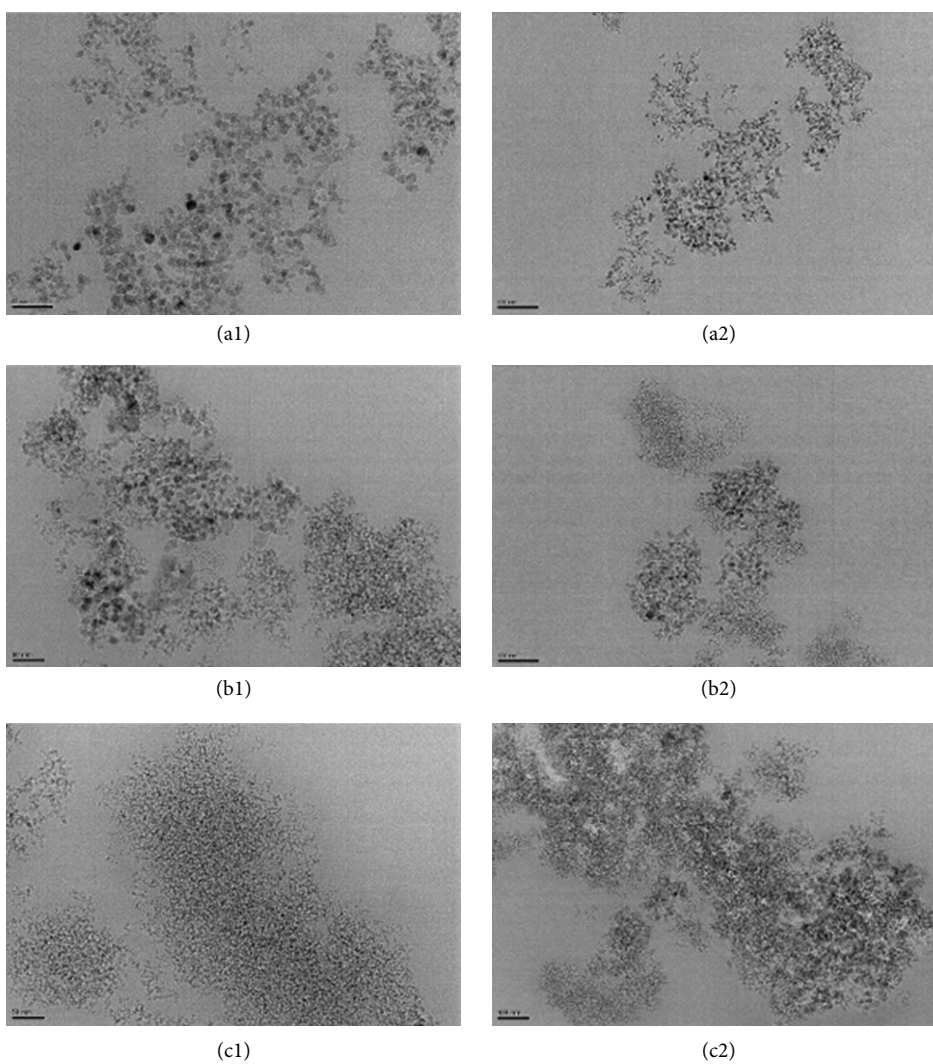


FIGURE 6: Representative transmission electron microscopy images of the nanodiamonds dispersed in the base material at varying contents: (a) 0.2, (b) 0.5, and (c) 1.0 wt. %.

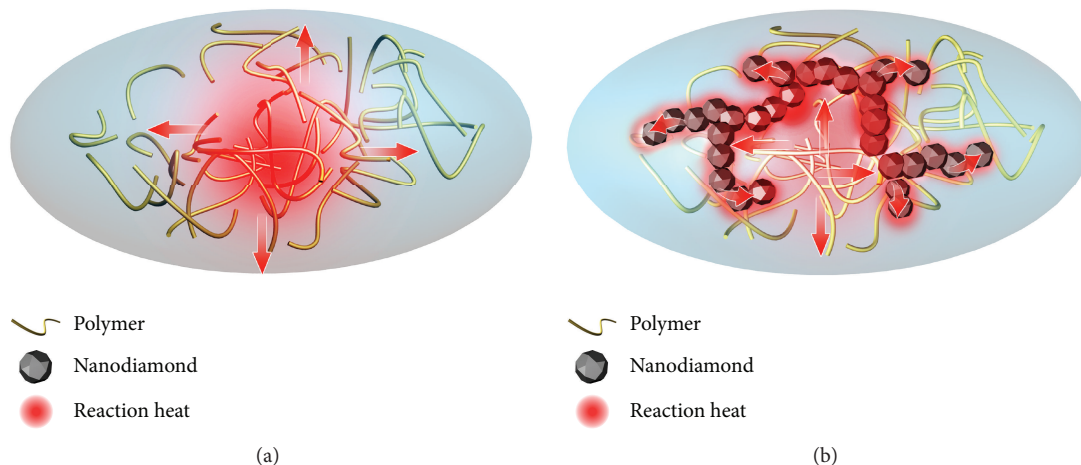


FIGURE 7: Heat dissipation model in the base material in the (a) absence and (b) presence of nanodiamonds.

TABLE 2: Content of MMA monomers in air for the base materials prepared with different nanodiamond contents.

Nanodiamond content (wt.%)	MMA monomer content in air ( $\text{g}/\text{m}^3$ )
0.0	0.337
0.5	0.201
1.0	0.137

materials prepared with varying nanodiamond contents; the associated chromatogram is shown in Figure 4. As observed from Table 2, the amount of volatilized MMA monomers decreased gradually with increase in the nanodiamond content. Therefore, adding nanodiamonds helps to reduce the amount of harmful volatilized gases. This effect can be attributed to the decrease in the local high temperature.

**3.6. Electron Microscopy Analysis.** Figure 5 shows representative scanning electron microscopy images of the nanodiamonds modified with a silane coupling agent. The nanodiamond particles were spherical with sizes between 5 and 10 nm and no visible edges. The specific surface area of the particles was typically  $300\text{--}400\text{ m}^2\text{ g}^{-1}$ , with a maximum of  $450\text{ m}^2\text{ g}^{-1}$ . Figure 6 shows transmission electron microscopy images of the nanodiamonds dispersed in the base material at varying contents. With increasing nanodiamond content, the distribution density of the nanodiamonds in the resin and the probability of occurrence and observed amount of the nanodiamonds increased. At a nanodiamond content of 0.2 wt.%, the nanodiamond particles were more loosely dispersed in the resin, and thus the distance between the particles and agglomerates was larger. When the nanodiamond content exceeded 0.2 wt.%, the amount and volume of the nanodiamond agglomerates significantly increased, thereby leading to reduced separation between the agglomerates [7, 8].

These results showed that the agglomeration of the nanodiamond particles increased with increasing nanodiamond

content. Furthermore, the transmission electron microscopy images revealed that the resin matrix penetrated the gaps between the nanodiamond agglomerates. Consequently, except for the microscopic chemical bonding between the nanodiamond agglomerates and the base resin material, the filling phenomenon resulted in macroscopic physical interactions, such as mechanical interlocking, which strengthened the connection between the diamond agglomerates and the base resin material.

As schematically illustrated in Figure 7, adding nanodiamonds to the base material led to a decrease in the peak temperature during the curing process of the base material. This decrease in temperature is due to the very high thermal conductivity of the nanodiamonds ( $\sim 2300\text{ W m}^{-1}\text{ K}^{-1}$ ). The local distribution of the nanodiamonds in the base material shows some network connections and agglomerates. This network structure can benefit from the nanodiamonds' high thermal diffusivity, which effectively dissipates and releases heat from high-temperature areas, thus reducing differences in the temperature field of the entire system. Therefore, adding nanodiamonds to the base material can improve the curing process and reduce the amount of volatilized monomer and therefore decrease the adverse effects on the environment. The current strategy provides a potential pathway for the processing and modification of prosthetic socket base materials.

## 4. Conclusions

The current findings show that adding a predetermined amount of nanodiamonds (between 0.1 and 1.0 wt.%) to the prosthetic socket base material can increase the glass transition temperature and improve the mechanical properties of the cured base material. With increasing nanodiamond contents, the glass transition temperature increased and the mechanical properties improved slightly. Owing to the high thermal conductivity of the nanodiamonds, the localized curing reaction heat was dissipated and released, affording a more uniform temperature field in the curing system.

Therefore, adding nanodiamonds can improve the curing process of the base material, reduce the amount of unreacted volatile monomer, and decrease the adverse effects of any unreacted volatile monomer on the working environment. This provides a potential for improving the method and safety for the processing and modification of prosthetic socket base materials.

### Conflict of Interests

The authors declare that there is no conflict of interests regarding the publication of this paper.

### References

- [1] Q. Wang, T.-W. Wang, and W. Wei, "Study on thickening characteristics and curing behavior of unsaturated polyester resin," *Engineering Plastics Application*, vol. 34, pp. 37–40, 2006.
- [2] X. Li, Y. Yan, and S. Mao, "Determination of storage life and gelation time of UPR," *China Synthetic Resin and Plastics*, vol. 20, no. 1, pp. 24–27, 2003.
- [3] Y.-J. Zhao and Z.-H. Xu, "Study on the determination of methyl methacrylate in air of workplace using solvent desorption gas chromatography," *Chinese Journal of Industrial Medicine*, vol. 23, pp. 152–154, 2010.
- [4] F.-L. Tang and W. Zhu, "Separation and determination of ethyl acrylate and methyl methacrylate in ambient air by gas chromatography," *Analysis and Testing Technology and Instruments*, vol. 6, pp. 115–118, 2000.
- [5] J. Yu, X. Huang, L. Wang et al., "Preparation of hyperbranched aromatic polyamide grafted nanoparticles for thermal properties reinforcement of epoxy composites," *Polymer Chemistry*, vol. 2, no. 6, pp. 1380–1388, 2011.
- [6] R. Qian, J. Yu, L. Xie, Y. Li, and P. Jiang, "Efficient thermal properties enhancement to hyperbranched aromatic polyamide grafted aluminum nitride in epoxy composites," *Polymers for Advanced Technologies*, vol. 24, no. 3, pp. 348–356, 2013.
- [7] Y.-Q. Chu, Y. Tong, F.-L. Huang, and T.-L. Zhang, "Structure and properties of boundary layer between nanodiamond and resin matrix," *Transaction of Beijing Institute of Technology*, vol. 33, no. 1, pp. 1–5, 2013.
- [8] Y.-Q. Chu, Y. Tong, T.-L. Zhang, and F.-L. Huang, "Mechanical properties of dental composite resins containing nanodiamond of different diameters," *Journal of Beijing Institute of Technology*, vol. 21, no. 1, pp. 19–22, 2012.
- [9] Y.-Q. Chu, Y. Tong, T.-L. Zhang, F.-L. Huang, and X.-Z. Wang, "Synthesis of nanodiamond reinforced dental composite resins and their mechanical properties," *Fullerenes, Nanotubes and Carbon Nanostructures*, vol. 20, pp. 628–632, 2012.
- [10] X.-G. Hu, X.-Y. Gu, Y. Tong et al., "Study on modified ultrafine-diamond reinforcing and toughening bis-phenol A dental composites," *New Chemical Materials*, vol. 34, pp. 60–62, 2006.
- [11] W. Yu, H. Xie, Y. Li, L. Chen, and Q. Wang, "Experimental investigation on the thermal transport properties of ethylene glycol based nanofluids containing low volume concentration diamond nanoparticles," *Colloids and Surfaces A: Physicochemical and Engineering Aspects*, vol. 380, no. 1–3, pp. 1–5, 2011.
- [12] H. Xie, W. Yu, and Y. Li, "Thermal performance enhancement in nanofluids containing diamond nanoparticles," *Journal of Physics D: Applied Physics*, vol. 42, Article ID 095413, 2009.
- [13] D. Wang, Y. Tong, Y. Li, Z. Tian, R. Cao, and B. Yang, "PEGylated nanodiamond for chemotherapeutic drug delivery," *Diamond and Related Materials*, vol. 36, pp. 26–34, 2013.
- [14] D.-J. Lim, M. Sim, L. Oh, K. Lim, and H. Park, "Carbon-based drug delivery carriers for cancer therapy," *Archives of Pharmacological Research*, vol. 37, no. 1, pp. 43–52, 2014.
- [15] V. N. Mochalin, A. Pentecost, X.-M. Li et al., "Adsorption of drugs on nanodiamond: toward development of a drug delivery platform," *Molecular Pharmaceutics*, vol. 10, no. 10, pp. 3728–3735, 2013.
- [16] J.-H. Liu, S.-T. Yang, X.-X. Chen, and H. Wang, "Fluorescent carbon dots and nanodiamonds for biological imaging: preparation, application, pharmacokinetics and toxicity," *Current Drug Metabolism*, vol. 13, no. 8, pp. 1046–1056, 2012.

## Research Article

# Design of Polymeric Nanofiber Gauze Mask to Prevent Inhaling PM<sub>2.5</sub> Particles from Haze Pollution

Xingzhou Li<sup>1</sup> and Yan Gong<sup>2</sup>

<sup>1</sup>Beijing No. 35 High School, Beijing 100032, China

<sup>2</sup>Department of Materials Science and Engineering, Beijing Institute of Fashion Technology, Beijing 100029, China

Correspondence should be addressed to Yan Gong; [clygy@bift.edu.cn](mailto:clygy@bift.edu.cn)

Received 23 February 2015; Accepted 1 April 2015

Academic Editor: Qichen Wang

Copyright © 2015 X. Li and Y. Gong. This is an open access article distributed under the Creative Commons Attribution License, which permits unrestricted use, distribution, and reproduction in any medium, provided the original work is properly cited.

Recently, PM<sub>2.5</sub> (particulate matter with diameter of 2.5 micron or less) has become a major health hazard from the polluted air in many cities in China. The regular gauze masks are used to prevent inhaling the PM<sub>2.5</sub> fine particles; however, those masks are not able to filter out the PM<sub>2.5</sub> because of the large porosity of the mask materials. Some well-prevented masks usually have poor breathability, which increases other health risks. In this study, a polysulfone based nanofiber for mask filtration material was synthesized by electrospinning. That nanofiber mask material was characterized by SEM, air permeability test, and PM<sub>2.5</sub> trapping experiment. The results indicate that nanofiber mask material can efficiently filter out the PM<sub>2.5</sub> particles and simultaneously preserve a good breathability. We attribute such improvement to the nanoscaled fibers, having the same porosity as that of regular gauze mask but with extremely reduced local interfiber space.

## 1. Introduction

PM<sub>2.5</sub> (particulate matter with diameter of 2.5 micron or less) in polluted air can directly go through the lung alveolar to cause many diseases including asthma [1]. Recently, many Chinese cities are covered by haze air. Figure 1 showed the polluted air in Beijing. The heavy metals adhered on PM<sub>2.5</sub> particles may even lead to severe chronic health problems such as cancer after long-term exposure under the particles contained environment [2].

In order to prevent inhaling PM<sub>2.5</sub> in haze, people wear regular gauze masks. Most of those masks are made of non-woven fabric, activated carbon, or cotton which has fiber diameter of several micrometers [3]. They have significant shortcoming of poor PM<sub>2.5</sub> rejection and low air permeability [4].

In this paper, a novel polymeric nanofiber masks were synthesized by electrospinning. Such masks based on nanofibers are expected to well prevent the PM<sub>2.5</sub> particles and maintain a good air permeability. These nanofibers can be potentially developed to high efficiency and low cost mask product.

## 2. Materials and Methods

**2.1. Experiment Materials.** Polysulfone, acetone, polyethylene oxide, and dimethyl acetamide were purchased from Beijing Chemical Factory, China. Medical clinic masks, medical operating room masks, ITO PM<sub>2.5</sub> masks, N95 respirator, and R95 masks were purchased from Tianjin Youkang medical and health care products factory. All chemicals were of analytical grade and were used without further purification.

**2.2. Procedure for Electrospinning.** Polysulfone solution was prepared at a concentration of 18 wt% by dissolving in DMAc/acetone (9:1) with vigorous stirring. The prepared solution was kept overnight without stirring under room temperature to remove air bubbles. For the electrospinning, the 18 wt% polysulfone solutions were filled into a syringe with a metal needle connected with a high-voltage power supply (Tianjin Dongwen High Voltage Co., China). The voltage is 13 KV and the distance between the needle and the aluminium foil is 13 cm. The polymer solution was fed at a constant rate of 0.4 mL/h by using a syringe pump.

TABLE 1: Electrospinning conditions.

Polymer	Solvent	Humidity	Flow rate	Voltage	Distance	Time
Polysulfone 1.8 g/polyethylene oxide 0.018 g	Dimethylacetamide 9 mL/acetone 1 mL	53%	0.4 mL/h	13 kV	13 cm	15 min
						30 min
						60 min



FIGURE 1: Typical haze in Beijing.

The nanofibers were collected on the surface of a non-woven PP on the grounded aluminium foil. The collective time of nanofibers was 15, 30, and 60 min. More detailed information was shown in Table 1.

**2.3. Morphology Observation.** The membranes were dried in vacuo and sputtered gold before observation. The morphology of nanofiber membranes was imaged by scanning electron microscopy (SEM, Hitachi T-1000, Japan).

**2.4. Permeability Simulation Test.** Permeability simulation test device mainly includes a pump, a pressure differential gauge, a meter, and bronchus. The nanofiber mats and the commercial masks as control group were clamped by a well-sealed testing chamber, which was connected with a syringe at top, install a pressure meter at the side exit. The bottom side of the chamber was open to the ambient air. Counterweights were placed on the syringe to adjust the pressure inside the testing chamber. The resulting pressure above the nanofiber mats was measured by the pressure meter.

**2.5. Intercept Rate Test.** Intercept experimental equipment was conducted in a nuclear particle counter (Model of CPC 3772 made in TSI Company). That counter can measure the concentration of particles (diameter between 10 and 2500 nm) in the air. The particle concentration in air represented the PM2.5 intercept rate of the filtration material.

**2.6. Data Analysis.** All data were means  $\pm$  SD from three independent experiments. Comparisons between multiple groups were performed with the ANOVA test by SPSS. *P* values less than 0.05 were considered statistically significant.

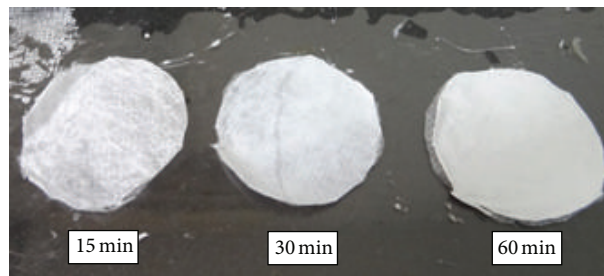


FIGURE 2: Nanomasks on non-woven fabrics.

### 3. Results

**3.1. Morphology Observation.** Figure 2 is the picture of nanofibers on the non-woven fabric. All the masks are white in color and homogeneously distributed on the non-woven fabric. The thickness of the electrospun fiber mats was at the rank of 15 min < 30 min < 60 min.

According to the SEM images, the nanofibers of 15 min electrospinning were about 500–800  $\mu\text{m}$  in diameter with random orientation and high porosity (Figure 2). The interdistance among the nanofibers is about 1–3  $\mu\text{m}$ . The nanofibers with 30 and 60 min electrospinning showed similar morphology to those of 15 min except for their higher thickness (data not shown).

**3.2. Permeability Test.** The permeability of the nanofiber masks was then compared with the commercial masks of disposable non-woven face mask, non-woven mask for operation room, Ito PM2.5, N95, and R95 (Figure 4). As listed in Table 2, the pressure drop of three nanofiber masks was 15 min < 30 min < 60 min. Compared with the commercial masks, the disposable non-woven face mask showed the lowest pressure drop, while the R95 had the highest barrier to air permeability. The low pressure drop indicated the good permeability.

**3.3. Intercept Rate Test of PM2.5 by Nanofiber Masks.** Table 3 showed the PM2.5 rejection capability of each mask in the intercept rate test. The rejecting ratio was calculated by the rejected particles/total particles in air. All the three nanofiber masks performed a high rejected effect of >90%, at the rank of 60 min > 30 min > 15 min. For the commercial available masks, the disposable non-woven face mask showed the poorest effect on PM2.5 rejection of 32.9%, which could not match the requirement of daily use. By contrast, the R95 mask for medical use in preventing virus permeability had

TABLE 2: The pressure drop statistics in permeability test.

Masks	Import (KP)	Export (KP)	Pressure drop (KPa)
Disposable non-woven face mask	1.23	1.52	$\Delta 0.29$
Non-woven mask for operation room	1.05	1.695	$\Delta 0.645$
Ito PM2.5	1.045	1.7	$\Delta 0.655$
N95	1.125	1.635	$\Delta 0.51$
R95	1.06	1.685	$\Delta 0.625$
Nanomask (15 minutes)	1.43	1.84	$\Delta 0.41$
Nanomask (30 minutes)	1.19	2.06	$\Delta 0.87$
Nanomask (60 minutes)	0.915	2.023	$\Delta 1.108$

TABLE 3: PM2.5 rejection by selected masks.

Sample	Average particle number	Rejection ratio
Indoor air (negative control)	$14452.9 \pm 320.6$	—
Disposable non-woven face mask	$9695.3 \pm 57.0$	32.9%
Non-woven mask for operation room	$499.2 \pm 7.8$	96.5%
ITO PM2.5	$2480.3 \pm 31.1$	82.8%
N95	$739.0 \pm 11.6$	94.9%
R95	$12.4 \pm 1.2$	99.9%
Nanomask (15 minutes)	$1318.8 \pm 23.6$	90.9%
Nanomask (30 minutes)	$476.7 \pm 8.5$	96.7%
Nanomask (60 minutes)	$82.2 \pm 3.5$	99.4%
Cellulose microfiltration membrane (positive control)	$0.3 \pm 0.1$	100.0%

an extremely high rejection of 99.9%, which is the highest one among the selected masks in our study.

#### 4. Discussion

In this study, a novel nanofiber mask was synthesized by electrospinning for preventing the PM2.5 from haze air. That nanofiber mask showed better performance than the commercial masks in both air permeability and PM2.5 rejection.

To make a clear comparison, the advantages and disadvantages of commercial masks have been summarized in Table 4. Most of these masks were made of non-woven fabric microfibers with large diameters of several micrometers [5]. The thin microfiber mask such as the disposable non-woven mask, though showed excellent air permeability, performed poor rejection on PM2.5 due to the insufficient thickness

of fibers and larger interfiber space. In contrast, the thick microfiber masks of Ito PM2.5 and N95 improved the rejecting ratio of PM2.5 to >80% which is enough for daily use. But they both had high resistance on air permeability which led to uncomfortable breathability in use. The R95 mask, which is commonly used in medical purpose, could well protect the doctors from virus infection. However, it was not suitable for preventing air pollution in daily use because of the extremely poor air permeability. The nanofiber mask with 15 min electrospinning had a high PM2.5 rejection of 90% and acceptable air permeability (Tables 2 and 3). Therefore, it is a good mask raw material for preventing haze air pollution.

The requirement on air permeability and PM2.5 rejection is a contradiction [6]. That means the high air permeability usually reduces the particle rejection of PM2.5 and vice versa. As shown in Figure 3, the nanofiber mask (15 min) displayed the largest difference between air permeability and PM2.5 rejection among these masks. We attribute that unique feature to the nanoscaled fiber size. At the same porosity, which indicates air permeability, the smaller fiber required higher quantity to achieve the same coverage as that of the bigger fiber. More fibers in the same area result in smaller interfiber space. From the SEM image in Figure 3, when the fiber scale is down to submicron, the interfiber space between the nanofibers is also reduced to micron scale, which is smaller than the PM2.5 size, consequently rejecting the PM2.5 passing efficiently.

#### 5. Conclusion

This study synthesized a polysulfone nanofiber for mask filtration material by electrospinning. The nanofiber mask material was characterized by SEM, air permeability test, and PM2.5 trapping experiment. This nanofiber mask material can efficiently filter out the PM2.5 particles and simultaneously preserve a good breathability. In this regard, this nanofiber based material would be made into the comfortable and effective mask to prevent inhaling the harmful particles in haze air pollution. The nanofiber masks could be developed to commercial available masks in the future.

TABLE 4: Comparison of different masks.

Name	Material	The scope of use and effect	Problem
Medical masks	Non-woven fabric	For hospital outpatient, disposable, good sanitary conditions	Interception effect of fine particles is poor
	Blended material	For the operation room, disposable, good sanitary conditions	Water vapor is poor, respiratory resistance is high
ItoPM2.5 masks	Thickened non-woven fabric	Dedicated to filter PM2.5	Respiratory resistance
N95 masks	Thickened non-woven fabric	Protection of professional occupation, preventing a flow HINI and microbial particles	Respiratory resistance, poor comfort
R95	Activated carbon	Used for industrial dust and trace organic gas entrapment	Respiratory resistance, poor comfort

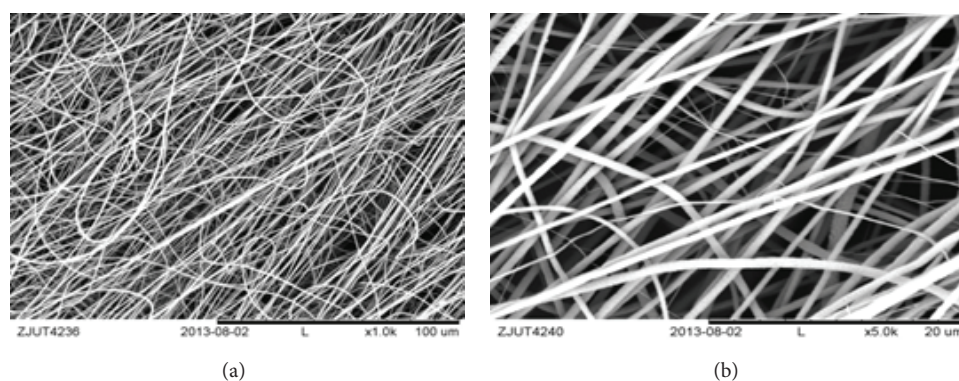
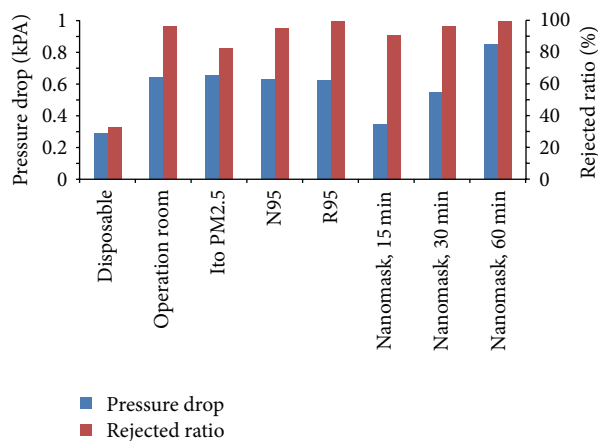
FIGURE 3: SEM images of masks after 15 min electrospinning. (a)  $\times 1000$  and (b)  $\times 5000$ .

FIGURE 4: Permeability and intercept rate comprehensive comparison.

### Conflict of Interests

The authors declare that there is no conflict of interests regarding the publication of this paper.

### Acknowledgements

The authors gratefully acknowledge the financial support of this study by Beijing Nova Program (no. 2014033) and NSFC (National Natural Science Foundation of China, no. 21002006). They thank Chong Shen and Yuanyuan Dai in Zhejiang University for their help on mask fabrication and testing.

### References

- [1] K. Yoon, B. S. Hsiao, and B. Chu, "Functional nanofibers for environmental applications," *Journal of Materials Chemistry*, vol. 18, no. 44, pp. 5326–5334, 2008.
- [2] A. Peters, D. W. Dockery, J. E. Muller, and M. A. Mittleman, "Increased particulate air pollution and the triggering of myocardial infarction," *Circulation*, vol. 103, no. 23, pp. 2810–2815, 2001.
- [3] Y. Li, K. Xiao, J. Luo, J. Lee, S. Pan, and K. S. Lam, "A novel size-tunable nanocarrier system for targeted anticancer drug delivery," *Journal of Controlled Release*, vol. 144, no. 3, pp. 314–323, 2010.
- [4] H.-J. Jin, S. V. Fridrikh, G. C. Rutledge, and D. L. Kaplan, "Electrospinning *Bombyx mori* silk with poly (ethylene oxide)," *Biomacromolecules*, vol. 3, no. 6, pp. 1233–1239, 2002.

- [5] S. Chen, M. Kong, S. Wang, D. Kong, and Z. Gu, "The electrostatic spinning technology vs its application in the field of biomedicine," *Chinese Journal of Biomedical Engineering*, vol. 30, pp. 120–130, 2011.
- [6] X. Qin and S. Wang, "The process principle, present situation and application prospect of electrostatic spinning of nano fibers," *Donghua University High-Tech Fiber and Application*, vol. 29, pp. 28–33, 2004.

## Research Article

# Effects of Nanoscale Carbon Black Modified by $\text{HNO}_3$ on Immobilization and Phytoavailability of Ni in Contaminated Soil

Jiemin Cheng, Lei Yu, Tong Li, Yuzhen Liu, Chengxiu Lu, Tingting Li, and Hanwei Wang

College of Population Resources and Environment, Shandong Normal University, Jinan 250014, China

Correspondence should be addressed to Jiemin Cheng; 1756736835@qq.com

Received 17 March 2015; Accepted 30 April 2015

Academic Editor: Qichen Wang

Copyright © 2015 Jiemin Cheng et al. This is an open access article distributed under the Creative Commons Attribution License, which permits unrestricted use, distribution, and reproduction in any medium, provided the original work is properly cited.

A surface-modified nanoscale carbon black (MCB) as Ni adsorbent in contaminated soil was prepared by oxidizing the carbon black with 65%  $\text{HNO}_3$ . The surface properties of the adsorbent were characterized by zeta potential analysis, scanning electron microscopy (SEM), and Fourier transform infrared spectroscopy (FTIRs). Batch experiments were conducted to evaluate the improvement of  $\text{Ni}^{2+}$  adsorption by MCB. Greenhouse cultivation experiments were conducted to examine the effect of MCB on the DTPA-extractable  $\text{Ni}^{2+}$  in soil,  $\text{Ni}^{2+}$  uptake of ryegrass shoot, and growth of ryegrass. Results indicated that MCB had much lower negative zeta potential, more functional groups for exchange and complexation of cation, and more heterogeneous pores and cavities for the adsorption of cation than the unmodified parent one (CB). MCB showed enhanced sorption capacity for Ni ( $q_{\max}$ ,  $49.02 \text{ mg}\cdot\text{g}^{-1}$ ) compared with CB ( $q_{\max}$ ,  $39.22 \text{ mg}\cdot\text{g}^{-1}$ ). Greenhouse cultivation experiment results showed that the biomass of ryegrass shoot and the Ni uptake of the ryegrass shoot were significantly increased and the concentrations of DTPA-extractable Ni in soil were significantly decreased with the increasing of MCB amount. It is clear from this work that the MCB had good adsorption properties for the Ni and could be applied in the in situ immobilization and remediation of heavy metal contaminated saline-alkali soils.

## 1. Introduction

Heavy metal pollution is a serious environmental problem. Refineries, mines, and fertilizers (exclusively phosphate) are the major sources of Ni dispersion in soil [1]. Nearly all the concentrations of Ni are higher than their background values of soil in some areas in China [2]. Due to the potential public health risk associated with intake, Ni has been a group of pollutants of much concern. Among the many remediation methods, in situ immobilization remediation successfully demonstrated its superiority for the remediation of farmland contaminated by heavy metals of low concentration [3–5]. The effectiveness of in situ immobilization remediation depends not only on a range of factors such as types of contaminants, reagents, soil conditions, and land use [6] but also on the physicochemical properties of the immobilization materials, so developing efficient, low-cost,

and environment-friendly immobilization materials is a key to successful application of remediation technology for the contaminated soils with lower concentration of heavy metals.

Because the nanoscale carbon black has large specific surface area, highly active adsorption sites, and good electric ability, considerable attention has been focused on developing and applying it in wastewater treatment [7, 8] and in situ immobilization remediation of contaminated soil [9, 10]. The nanoscale carbon black is a hydrophobic and nonpolar adsorbent, and it has strong adsorption ability to nonpolar organic compounds [11–15]. However, the nanoscale carbon black has poor adherence to heavy metal ions. In fact, research has shown that the maximum amounts of Pb(II) adsorption by the nanoscale carbon black were lower than expandable clay mineral and humic acid [16, 17]. Surface modification of the nanoscale carbon black by appropriate physical and chemical treatments could improve its adsorption capacities for heavy

metal ions [18]. The adsorption quantities of Cu(II) or Cd(II) on a surface-modified nanoscale carbon black oxidized with 65% HNO<sub>3</sub> were significantly increased [19, 20]. It had been found that the surface-modified nanoscale carbon black significantly reduced the bioavailability of Cu and Zn in red earth with lower pH (3.99) [21, 22]. When the surface-modified nanoscale carbon was added into acidic soil, the pH value of soil increased, and then the bioavailability of heavy metals in soil was reduced. After treating with acid, the nanoscale carbon black has a pH value of about 5.5, but its effect in higher pH saline-alkali soil (7.76) is unknown.

The major objective of the present study is to compare the surface properties and the adsorption capacity between a surface-modified nanoscale carbon black (MCB) and the unmodified parent one (CB) by batch experiment and to investigate the feasibility of using the modified nanoscale carbon black as immobilization material for Ni-contaminated saline-alkali soil by cultivation experiment. This work provided a proof for an application of the MCB in in situ immobilization remediation of metals contaminated saline-alkali soils.

## 2. Materials and Methods

**2.1. Modification of Nanoscale Carbon Black.** A commercial nanoscale carbon black (CB) with particle size of 20–70 nm was purchased from Jinan Carbon Black Factory, Shandong Province, China. This carbon black was further oxidized with 65% HNO<sub>3</sub> for modification by refluxing 10 g of carbon black with 150 mL HNO<sub>3</sub> (65%) in a conical flask at 110°C for 2 h. The modified nanoscale carbon black (MCB) was filtered, washed with deionized water until the pH of the filtrate became stable (pH is about 5.5), and finally dried in a vacuum oven at 110°C for 24 h [19].

### 2.2. Surface Properties

**2.2.1. Zeta Potential of the CB or MCB.** The CB and MCB suspensions (0.4 g·L<sup>-1</sup>) containing 0.01 M NaNO<sub>3</sub> as background electrolyte were prepared at different pH values. The suspensions were dispersed ultrasonically at a frequency of 40 kHz and a power of 300 W for 1 h and then shaken for 20 h at 25°C. After being equilibrated for two days, the zeta potential was measured using a JS94G+ microelectrophoresis instrument (Shanghai Zhongchen Digital Technique Equipment Ltd. Co., Shanghai, China) and the suspension pH was also determined.

**2.2.2. Fourier Transform Infrared Spectroscopy (FTIRs) of the CB or MCB.** Infrared spectra (IR) of the CB or MCB were recorded using a Perkin-Elmer 2000 Fourier transform infrared spectroscopy (FTIRs) spectrometer fitted with a deuterated triglycine sulfate (DTGS) detector covering the frequency range of 500–4000 cm<sup>-1</sup>. The sample cell was purged with nitrogen gas throughout data collection to exclude carbon dioxide and water vapor. Ten milligrams of the dried samples was evenly dispersed in 200 mg of spectroscopic grade KBr to record the spectra.

**2.2.3. SEM (Scanning Electron Microscopy) of the CB or MCB.** The samples were placed on the exposed upper surface of double-sided carbon tape attached to standard AL mounting stubs. The SEM analyses were carried out using a LEO 982 field-emission SEM with an Oxford energy dispersive X-ray analyzer.

### 2.3. Batch Adsorption Experiments

**2.3.1. Adsorption Kinetics Experiments.** Ni adsorption kinetics experiments were conducted by mixing the suspensions containing 0.1000 g CB or MCB, 30 mL Ni standard solution (180 mg Ni<sup>2+</sup>·L<sup>-1</sup>), and 0.01 M NaCl as electrolyte in 12 PTFE centrifuge tubes. Tubes were sealed and shaken at the temperature of 25°C for 20 min, 30 min, 40 min, 60 min, 90 min, 120 min, 180 min, 300 min, 420 min, 600 min, 720 min, and 900 min. Finally, the amount of Ni<sup>2+</sup> was determined after centrifuging and filtering through 0.45 μm membrane. In the meantime, the controlled experiments were carried out by the same procedure as above except utilizing the CB instead of MCB. Both experiments of MCB and CB were performed in duplicate. Kinetic curves of the adsorption were made at last. The residual Ni<sup>2+</sup> concentration in solution samples was measured using an atomic absorption spectrometry (Thermo Orion 9609 BN) according to the standard method [23].

**2.3.2. Adsorption Isotherms Experiments.** The adsorption isotherms were obtained by mixing the suspensions, containing 0.1000 g CB or MCB, 30 mL Ni standard solution (0, 20, 40, 60, 80, 100, 120, 150, and 180 mg Ni<sup>2+</sup>·L<sup>-1</sup>), and 0.01 M NaCl as electrolyte in 50 mL PTFE (polytetrafluoroethylene) centrifuge tubes. Tubes were sealed and shaken at the temperature of 25°C for 2 h. Finally, the amount of Ni<sup>2+</sup> was determined after centrifuging and filtering through 0.45 μm membrane. In the meantime, the controlled experiments were carried out by the same procedure as above except utilizing the CB instead of MCB. Adsorption isotherms for the adsorption were made at last.

### 2.4. Greenhouse Experiments

**2.4.1. Collection of Soil Samples and Preparation.** A saline-alkali soil of plough layers (0–20 cm) was sampled from Dongying (Shandong Province, China). The saline-alkali soil used in the research is from the Yellow River alluvial parent material. The soil sample was air-dried and sieved (2 mm mesh). The general properties of the soil were pH 7.76, salt content 0.35%, cation exchange capacity (CEC) 9.29 cmol·kg<sup>-1</sup>, organic matter (OM) 8.34 g·kg<sup>-1</sup>, clay content up to 18.5%, Yellow River alluvial parent materials, Ni 22.61 mg·kg<sup>-1</sup>, and Cd 0.49 mg·kg<sup>-1</sup>.

The following properties were analyzed: pH (by CaCl<sub>2</sub> extraction), organic matter (by H<sub>2</sub>SO<sub>4</sub>-K<sub>2</sub>Cr<sub>2</sub>O<sub>7</sub> with external heating), CEC (by Kjeldahl digestion), available Ni (extracted by DTPA, pH 7.3), and total Ni (by HNO<sub>3</sub>-HClO<sub>4</sub>-HF extraction), followed by atomic absorption spectrophotometry (AAS) [24].

**2.4.2. Experimental Design and Procedures.** The soil environmental quality standards value of China for Ni in a saline-alkali soil is lower than  $60 \text{ mg}\cdot\text{kg}^{-1}$  [25]. The soil background value of Ni is about  $22.61 \text{ mg}\cdot\text{kg}^{-1}$  in the investigation area of this paper, and the Ni content in contaminated soil ranged from  $80 \text{ mg}\cdot\text{kg}^{-1}$  to  $100 \text{ mg}\cdot\text{kg}^{-1}$ .

$\text{Ni}^{2+}$  was added to soil and amended to contain  $100 \text{ mg Ni kg}^{-1}$  by adding appropriate concentrations of  $\text{Ni}(\text{NO}_3)_2$ . Deionised water was added to the soils to achieve a moisture content of 70% of field capacity. To ensure even dispersion of Ni, soils were thoroughly mixed while adding  $\text{Ni}(\text{NO}_3)_2$  and water. The soils were incubated at room temperature (at about  $20^\circ\text{C}$ ) for 2 months, allowing  $\text{Ni}^{2+}$  to be distributed into various fractions. During the period, soil moisture content was carefully monitored.

The MCB of 0, 0.5%, and 1% was added into soil, mixed thoroughly, and placed into pots (1.5 kg per pot). For each pot, 0.33 g urea and 0.35 g  $\text{K}_2\text{HPO}_4$  were added as fertilizer and mixed thoroughly. There were three replicates for each treatment, with 9 pots in total. All pots were adjusted regularly to 70% of field water-holding capacity using deionized water.

Fifteen well-germinated ryegrass seeds (*Lolium multiflorum*) (obtained from the College of Life Sciences, Shandong Normal University, China) were sowed in each pot. The pots were placed in the greenhouse under a random block design and the ryegrass shoot was harvested after 60 days (approximately 0.5 cm aboveground), and the shoot was separated, washed, and weighed after adhering water was removed with filter paper. The ryegrass shoot was digested by  $\text{HCl-HNO}_3\text{-HClO}_4$ , and Ni was determined by AAS [24]. The soil subsamples were air-dried and ground to pass through a 1-mm sieve before use.

**2.5. Statistical Methods.** Arithmetic means and standard errors of the mean were calculated using Microsoft Excel *t*-test (unequal variance assumed to be  $P < 0.05$  was used to determine the difference between treatments with and without MBC) [26].

### 3. Results and Discussion

#### 3.1. Surface Characteristics of CB and MCB

**3.1.1. The Zeta Potential of the CB and MCB.** The zeta potentials of both CB and MCB were shown in Figure 1. MCB has more negative charge than CB, and the zeta potential decreased from  $-20 \text{ mV}$  to  $-60 \text{ mV}$  from pH 3 to 8. Zeta potential is widely used to quantify the magnitude of the electrical charge in the double layer [27]. The MCB particles had lower zeta potential values than the CB particles at the same pH and should have higher adsorption affinity for  $\text{Ni}^{2+}$  than CB.

**3.1.2. The FTIRs of the CB or MCB.** The FTIRs analyses were conducted to identify characteristic functional groups. The IR spectra of CB and MCB were presented in Figure 2. Compared with CB, MCB exhibited some characteristic peaks at wavenumbers of 1580, 1709, and  $3424 \text{ cm}^{-1}$ , which

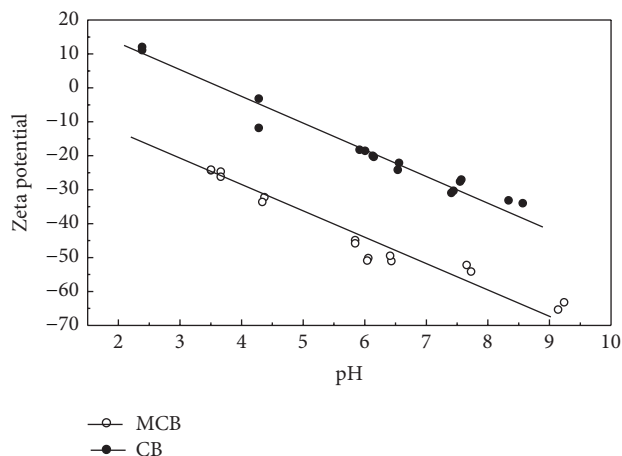


FIGURE 1: Zeta potential of MCB and CB.

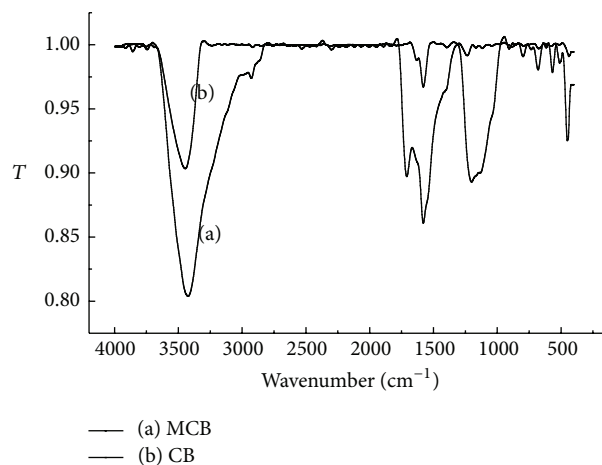


FIGURE 2: Infrared spectrum of MCB and CB.

were associated with hydroxyl groups or carbonyl groups, carboxylic acids, and hydroxyl groups [28], respectively. As it can be seen from Figure 2, the absorption of phenol hydroxyl C-O, which is at wavenumbers of  $1250 \text{ cm}^{-1}$ , was increased compared with CB. The increased amounts of these functional groups resulted in the increasing surface cation exchange and complexation capacity of MCB [29].

**3.1.3. The SEMs of CB or MCB.** Figure 3 showed SEM images of CB and MCB. The pore structure had not been observed from the SEM image of CB and exhibited nonadhesive appearance and formation of agglomerates. Fusing of aggregates by van der Waals forces resulted in the formation of new structures—agglomerates, as previously described in the literature [30]. Comparing with CB, MCB particles had heterogeneous pores and cavities. CB is produced by partial combustion of petroleum or natural gas, and its pH is normally neutral to basic (pH from 6.2 to 9.6), depending on the feedstock and pyrolysis conditions used in various studies [31, 32]. The CB surfaces morphology change depends on the different treating methods. For example, the acetic

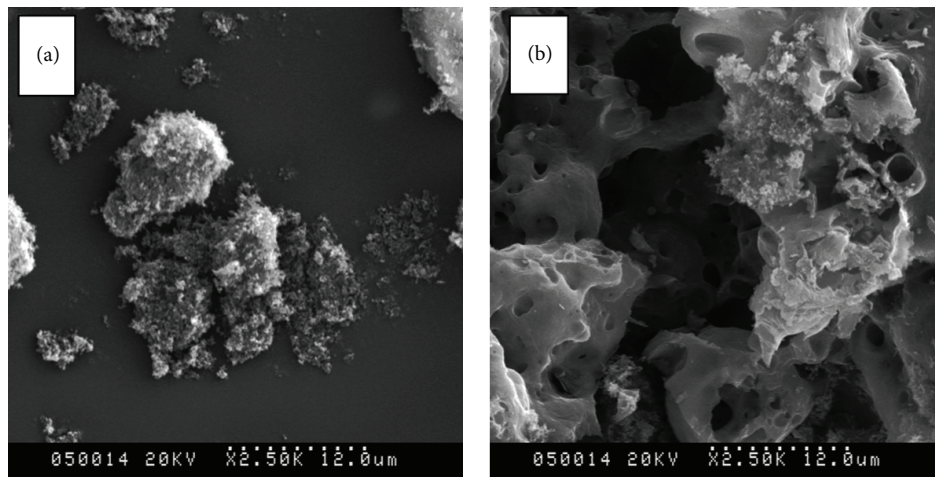


FIGURE 3: (a) SEM image of CB. (b) SEM image of MCB.

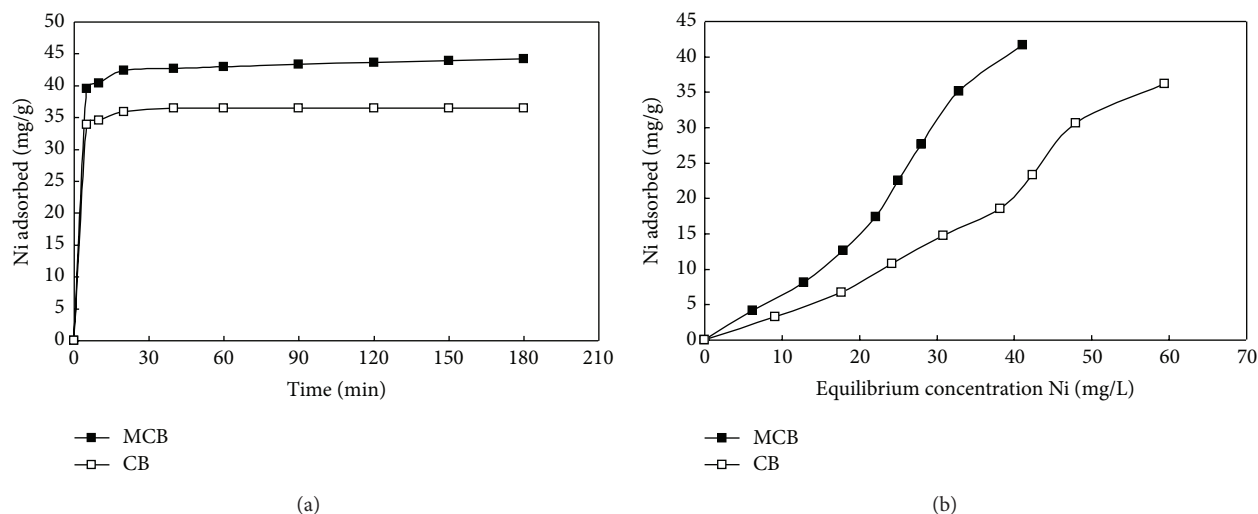


FIGURE 4: Adsorption kinetics (a) and adsorption isotherms (b) of Ni on MCB and CB at pH = 7.0 and  $T = 25^{\circ}\text{C}$ .

acid modification reduces the number of cracks and pores on CB surfaces, which are clogged by adsorbed acetic acid [33]. Therefore, selecting an appropriate acid is crucial. In our study, after treating with nitric acid, pores and caves formed on the MCB surface. Those pores and caves provided larger exposed surface area for the adsorption of cation.

### 3.2. Adsorption Kinetics and

#### Adsorption Isotherms of CB or MCB

**3.2.1. Adsorption Kinetics.** Figure 4(a) showed the adsorption kinetic curves of Ni on CB and MCB at pH 7.0. Ni adsorbed by CB or MCB occurred rapidly and reached equilibrium within about 20 minutes. The pseudo-first-order kinetic equation [34] and pseudo-second-order kinetic equation [35] were applied to fit the adsorption kinetic data in Figure 4(a).

It is clear from Table 1, and the pseudo-first-order model did not adequately fit the experimental data because all

the  $R^2$  of CB or MCB is 0.5077 or 0.6919. However, the pseudo-second-order model for adsorption of Ni onto CB or MCB agrees well with experimental data because all values of  $R^2$  are greater than 0.999. Liu and Cheng [20] reported that the adsorption kinetic model of  $\text{Cu}^{2+}$  and  $\text{Cd}^{2+}$  on CB or MCB followed pseudo-second-order model well. In general, the pseudo-second-order rate expression was used to describe chemisorption involving valency forces through the sharing or exchange of electrons between the adsorbent and adsorbate as covalent forces and ion exchange [36]. The much lower rate of constant  $k_2$  for MCB (i.e., 0.01799) than for CB (i.e., 0.1532) also indicated the much faster adsorption kinetics of  $\text{Ni}^{2+}$  on CB than on MCB. It could be ascribed to more heterogeneous pores and cavities on the MCB particles than CB (Figure 3) [19]. The rate of  $\text{Ni}^{2+}$  into internal surface sites of the CB or MCB was slower than on external surface sites. In most cases, the pseudo-second-order chemical reaction kinetics provide the best

TABLE 1: The best-fit model parameters for adsorption of  $\text{Ni}^{2+}$  on CB and MCB.

Sorbents	Pseudo-first-order model			Pseudo-second-order model			Langmuir isotherm			Freundlich isotherm		
	$q_{1e}$ (mg/g)	$k_1$ ( $\text{min}^{-1}$ )	$R_1^2$	$q_{2e}$ (mg/g)	$k_2$ ( $\text{g}/(\text{mg}\cdot\text{min})$ )	$R_2^2$	$q_{\max}$ (mg/g)	$K_L$ ( $\text{L}\cdot\text{kg}^{-1}$ )	$R^2$	$K_F$ (mg/g)	$n$	$R^2$
CB	1.220	0.1101	0.5077	36.49	0.1532	0.9999	39.22	0.008901	0.9205	6.104	0.7576	0.9823
MCB	3.032	0.1010	0.6919	44.25	0.01799	0.9999	49.02	0.01200	0.8272	2.934	0.7740	0.9926

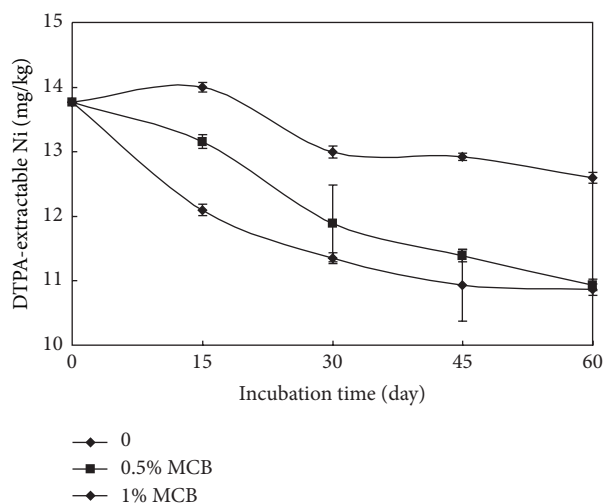


FIGURE 5: Effect of MCB on DTPA-extractable Ni in soil.  $\text{Ni}^{2+}$  was added to soil at the ratio of  $100 \text{ mg}\cdot\text{kg}^{-1}$  and the MCB was added at the ratio of 0, 0.5%, and 1%, respectively.

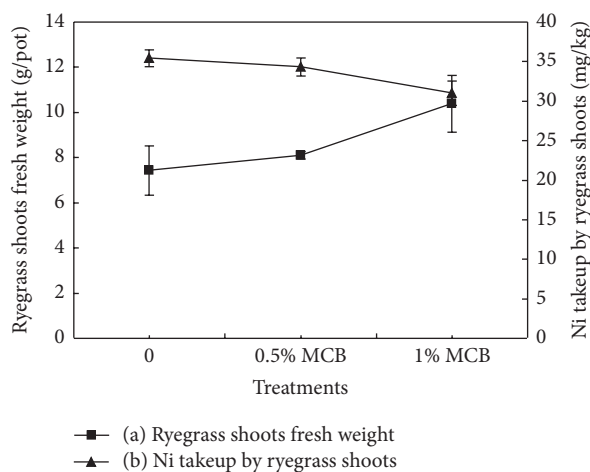


FIGURE 6: Effect of MCB on the biomass of ryegrass shoots and Ni uptake by ryegrass shoots.  $\text{Ni}^{2+}$  was added to soil at the ratio of  $100 \text{ mg}\cdot\text{kg}^{-1}$  and the MCB was added at the ratio of 0, 0.5%, and 1%, respectively.

correlation of the experimental data, whereas the pseudo-first-order model proposed fits the experimental data well for an initial period of the first reaction step only [37]. Cheng et al. [38] reported that the adsorption of  $\text{Cu}^{2+}$  or  $\text{Cd}^{2+}$  on MCB reached equilibrium rapidly within 30 minutes and more than 90% of the equilibrium adsorption amount.

3.2.2. *Adsorption Isotherms.* Figure 4(b) illustrated the adsorption isotherms of  $\text{Ni}^{2+}$  on the CB and MCB at pH 7.0. The *Freundlich* isotherm and *Langmuir* isotherm were applied to fit the adsorption isotherm data.

The best-fit parameters are listed in Table 1. The  $R^2$  values suggested that the *Freundlich* isotherm described the adsorption data better than the *Langmuir* isotherm. The value of  $q_{\max}$  (maximum adsorption capacity) for CB was  $39.22 \text{ mg}\cdot\text{g}^{-1}$ , and for MCB it was  $49.02 \text{ mg}\cdot\text{g}^{-1}$ . Literature data confirm that the affinity of the carboxylic functional groups for metal ions is very high [39], so the increase of adsorbed capacity might be attributed to the increase of oxygenic functional groups and the consequent increase of surface cation exchange and complexation capacity of the MCB [29]. It is consistent with the conclusion that oxidation increased the functional groups on CB surfaces and then increased the maximum adsorption capacity of heavy metals. Various methods such as acid treatment, base treatment, impregnation treatment, ozone treatment, surfactant treatment, plasma treatment, and microwave treatment have been studied to develop surface-modified activated carbons [40]. Ankica and Jadranka results showed that modification by acetic acid increases the adsorption capacity of carbon black from  $18.3823$  to  $86.9566 \text{ mg Ni(II)} \text{ g}^{-1}$ , though the specific surface area of carbon black is decreased, and its surface becomes more homogeneous after modification [33]. The Ni adsorption capacity on microwave and thermally heated activated carbon was  $12.00$  and  $8.42 \text{ mg}\cdot\text{g}^{-1}$ , respectively [41]. The  $q_{\max}$  is different in different modification methods, so it is necessary to further study the adsorption mechanism of CB modified by different methods.

### 3.3. Effect of MCB on Available $\text{Ni}^{2+}$ in Soil

3.3.1. *DTPA-Extractable Ni in Soil.* The DTPA (diethylene triamine pentaacetic acid) extraction method has been employed well to estimate the metal availability for plants in neutral to calcareous soils [42]. The concentrations of DTPA-extractable Ni in soils were significantly decreased with the increase of incubation day, when  $\text{Ni}^{2+}$  was added to soil at the ratio of  $100 \text{ mg}\cdot\text{kg}^{-1}$  and the MCB was added at the ratio of 0, 0.5%, and 1%, respectively (Figure 5). Compared with non-MCB, the concentrations of DTPA-Ni decreased by 12.15% and 13.58% when the MCB was added at ratios of 0.5% and 1% at 15 days ( $P < 0.05$ ) and decreased by 13.18% and 13.74% at 60 days. Cui et al. [43] study showed that CB amendment offers a basic option to reduce Cd and Pb bioavailability and change the fractions, when the CB was applied at rates of 0, 10, 20, and 40 tons per hectare. Cheng et al. [22] study showed

that the concentrations of DTPA-extractable Cu and Zn in soil were significantly decreased by addition of MCB.

Notably, the results mentioned above were obtained in lower pH, but the effects of MCB on the bioavailability were obtained in higher pH saline-alkali soil in this paper. pH of biochar is normally neutral to basic (pH from 6.2 to 9.6), depending on the feedstock and pyrolysis conditions used in various studies [31, 32]. When biochar is added in acidic soil, the pH value of soil is increased and then reduces the bioavailability of heavy metals in soil. However, the pH value of MCB is about 5.5, and the pH value of alkaline soil is about 7.8. The mechanism of effect bioavailability of heavy metals in soil may be different between biochar and MCB. The effect mechanism of MCB on the bioavailability of heavy metals in soil may be by adsorption and chelation, because it has lower negative zeta potential [19] and more hydroxyl groups or carboxyl groups, carboxylic acids, and hydroxyl groups [28].

**3.3.2. Ryegrass Shoots Biomass and Ni Uptake of Ryegrass Shoots.** Adding MCB significantly increased the biomass of ryegrass shoots, and they increased with the increase of MCB added amount, when  $\text{Ni}^{2+}$  was added to soil at the concentration of  $100 \text{ mg}\cdot\text{kg}^{-1}$  and the MCB was added at the ratio of 0, 0.5%, and 1%, respectively (Figure 6). Compared with non-MCB, the MCB groups showed the fresh weight of ryegrass shoots increased by 9.03% and 39.75%, respectively ( $P < 0.05$ ). The Ni uptake of the ryegrass shoots decreased with the increase of the MCB (Figure 6). Compared with non-MCB, the Ni uptake of the ryegrass shoots was not significantly different when the MCB addition was in 0.5% and significantly different ( $P < 0.05$ ) when the MCB addition was in 1% and the Ni uptake of the ryegrass shoots decreased by 12.48%.

Previous works indicated that the concentrations of DTPA-extractable heavy metals in soil were positive linearly correlated with the uptake heavy metals by plant [42]. Méndez et al. [44] suggested that the risk of leaching of Cu, Ni, and Zn was lower in the soil treated with biochar and biochar amended samples also reduced plant availability of Ni, Zn, Cd, and Pb. Application of chicken manure-derived biochar significantly reduced  $\text{NH}_4\text{NO}_3$  extractable Cd, Cu, and Pb concentrations of soils and increased plant dry biomass by 353 and 572% for shoot and root [45]. Cheng et al. [22] reported that the Cu and Zn uptake of the ryegrass shoots decreased by 34.98% and 14.52% in acid soil, comparing with non-MCB. In this study, the concentrations of DTPA-extractable Ni in soils were significantly decreased with the increment of MCB, and when the MCB addition was in 1%, the Ni uptake by ryegrass shoots decreased. The carbon black modified by this method is a potential application for the in situ immobilization remediation of heavy metal contaminated saline-alkali soil.

## 4. Conclusions

It is clear from this work that the nanoscale carbon black modified by  $\text{HNO}_3$  (MCB) has lower negative zeta potential

than the CB, more functional groups for exchange and complexation of cation and heterogeneous pores and cavities for the adsorption of cation than unmodified CB. The MCB had much higher  $q_{\text{max}}$  ( $49.02 \text{ mg}\cdot\text{g}^{-1}$ ) of nickel than the CB ( $39.22 \text{ mg}\cdot\text{g}^{-1}$ ) and showed very good adsorption and complexation properties for  $\text{Ni}^{2+}$  in soil. The MCB could be applied for the in situ immobilization remediation of heavy metal contaminated soils.

## Conflict of Interests

The authors declare that there is no conflict of interests regarding the publication of this paper.

## Acknowledgments

The authors would like to thank the National Natural Science Fund Committee, China (41171251), and the Ph.D. Programs Foundation of the Ministry of Education of China (20103704110001) for financial support.

## References

- [1] S. P. McGrath, "Chromium and nickel," in *Heavy Metals in Soils*, B. J. Alloway, Ed., pp. 152–178, Blackie, New York, NY, USA, 1995.
- [2] B. Wei and L. Yang, "A review of heavy metal contaminations in urban soils, urban road dusts and agricultural soils from China," *Microchemical Journal*, vol. 94, no. 2, pp. 99–107, 2010.
- [3] T. A. Martin and M. V. Ruby, "Review of *in situ* remediation technologies for lead, zinc, and cadmium in soil," *Remediation Journal*, vol. 14, no. 3, pp. 35–53, 2004.
- [4] M. A. Hashim, S. Mukhopadhyay, J. N. Sahu, and B. Sen-gupta, "Remediation technologies for heavy metal contaminated groundwater," *Journal of Environmental Management*, vol. 92, no. 10, pp. 2355–2388, 2011.
- [5] Z. Yao, J. Li, H. Xie, and C. Yu, "Review on remediation technologies of soil contaminated by heavy metals," *Procedia Environmental Sciences*, vol. 16, pp. 722–729, 2012.
- [6] M. C. Jung, "Heavy metal concentrations in soils and factors affecting metal uptake by plants in the vicinity of a Korean Cu-W mine," *Sensors*, vol. 8, no. 4, pp. 2413–2423, 2008.
- [7] C. Wu, X. Zhang, and G. Li, "Sorption of  $\text{Hg}^{2+}$ ,  $\text{As}^{3+}$ ,  $\text{Pb}^{2+}$  and  $\text{Cd}^{2+}$  by black carbon," *Journal of Agro-Environment Science*, vol. 26, no. 2, pp. 770–774, 2007.
- [8] B. Gong, Y. Qiu, Y. Zhao, and M. Huang, "Laboratory study on adsorption of methylene blue on black carbon in aqueous solution," *Environmental Science & Technology (China)*, vol. 32, no. 11, pp. 18–23, 2009 (Chinese).
- [9] L. Beesley, E. Moreno-Jiménez, J. L. Gomez-Eyles, E. Harris, B. Robinson, and T. Sizmur, "A review of biochars' potential role in the remediation, revegetation and restoration of contaminated soils," *Environmental Pollution*, vol. 159, no. 12, pp. 3269–3282, 2011.
- [10] J. Paz-Ferreiro, H. Lu, S. Fu, A. Méndez, and G. Gascó, "Use of phytoremediation and biochar to remediate heavy metal polluted soils: a review," *Solid Earth*, vol. 5, no. 1, pp. 65–75, 2014.
- [11] M. T. O. Jonker and A. A. Koelmans, "Sorption of polycyclic aromatic hydrocarbons and polychlorinated biphenyls to soot

- and soot-like materials in the aqueous environment: mechanistic considerations," *Environmental Science and Technology*, vol. 36, no. 17, pp. 3725–3734, 2002.
- [12] H. Bärning, T. D. Bucheli, D. Broman, and Ö. Gustafsson, "Soot-water distribution coefficients for polychlorinated dibenzo-*p*-dioxins, polychlorinated dibenzofurans and polybrominated diphenylethers determined with the soot cosolvency-column method," *Chemosphere*, vol. 49, no. 6, pp. 515–523, 2002.
- [13] G. Cornelissen and Ö. Gustafsson, "Sorption of phenanthrene to environmental black carbon in sediment with and without organic matter and native sorbates," *Environmental Science and Technology*, vol. 38, no. 1, pp. 148–155, 2004.
- [14] X.-Y. Yu, G.-G. Ying, and R. S. Kookana, "Sorption and desorption behaviors of diuron in soils amended with charcoal," *Journal of Agricultural and Food Chemistry*, vol. 54, no. 22, pp. 8545–8550, 2006.
- [15] S.-L. Wang, Y.-M. Tzou, Y.-H. Lu, and G. Sheng, "Removal of 3-chlorophenol from water using rice-straw-based carbon," *Journal of Hazardous Materials*, vol. 147, no. 1-2, pp. 313–318, 2007.
- [16] K. Guo and Y. Ma, "Research on adsorption and affecting factors of  $Pb^{2+}$  on several clay minerals," *Geology/Geochemistry*, vol. 4, pp. 109–113, 1997.
- [17] G. Li, S. Wei, and S. Mou, "Adsorptive characteristics and influence factors of humic acid on lead in soil," *Journal of Agro-Environment Science*, vol. 23, no. 2, pp. 308–312, 2004.
- [18] Y. Fan, B. Wang, and L. Wang, "Surface characteristics of modified carbons and its adsorption performance of heavy metal ions," *Environmental Chemistry*, vol. 20, no. 5, pp. 437–443, 2001 (Chinese).
- [19] D.-M. Zhou, Y.-J. Wang, H.-W. Wang, S.-Q. Wang, and J.-M. Cheng, "Surface-modified nanoscale carbon black used as sorbents for Cu(II) and Cd(II)," *Journal of Hazardous Materials*, vol. 174, no. 1–3, pp. 34–39, 2010.
- [20] Y.-Z. Liu and J.-M. Cheng, "Adsorption kinetics and isotherms of Cu (II) and Cd(II) onto oxidized nano carbon black," *Advanced Materials Research*, vol. 529, pp. 579–584, 2012.
- [21] H.-W. Wang, Y.-J. Wang, J.-H. Chen, S.-Q. Wang, J.-M. Cheng, and D.-M. Zhou, "Application of modified nano-particle black carbon for the remediation of soil heavy metal pollution," *China Environmental Science*, vol. 29, no. 4, pp. 431–436, 2009.
- [22] J.-M. Cheng, Y.-Z. Liu, and H.-W. Wang, "Effects of surface-modified nano-scale carbon black on Cu and Zn fractionations in contaminated soil," *International Journal of Phytoremediation*, vol. 16, no. 1, pp. 86–94, 2014.
- [23] APHA, *Standard Methods*, American Public Health Association, Washington, DC, USA, 19th edition, 1995.
- [24] R. H. Shi, *The Analytical Methods of Soil Agricultural Chemistry*, Chinese Agricultural Press, Beijing, China, 1996.
- [25] SEPA, "Environmental quality standard for soils," GB 15618-1995, State Environmental Protection Administration of the People's Republic of China, Beijing, China, 1995, (Chinese).
- [26] P. Armitage and G. Berry, *Statistical Methods in Medical Research*, Blackwell Scientific Publications, London, UK, 3rd edition, 1994.
- [27] R. J. Hunter, *Zeta Potential in Colloid Science: Principles and Applications*, Academic Press, London, UK, 1981.
- [28] A. Stafiej and K. Pyrzynska, "Adsorption of heavy metal ions with carbon nanotubes," *Separation and Purification Technology*, vol. 58, no. 1, pp. 49–52, 2007.
- [29] Y.-H. Li, J. Ding, Z. K. Luan et al., "Competitive adsorption of  $Pb^{2+}$ ,  $Cu^{2+}$  and  $Cd^{2+}$  ions from aqueous solutions by multiwalled carbon nanotubes," *Carbon*, vol. 41, no. 14, pp. 2787–2792, 2003.
- [30] T. C. Gruber, T. W. Zerda, and M. Gerspacher, "Three-dimensional morphology of carbon black aggregates," *Carbon*, vol. 31, no. 7, pp. 1209–1210, 1993.
- [31] F. G. A. Verheijen, S. Jeffery, A. C. Bastos, M. van der Velde, and I. Diafas, "Biochar application to soils—a critical scientific review of effects on soil properties, processes and functions," EUR 24099 EN, Office for the Official Publications of the European Communities, Luxembourg, 2009.
- [32] F. Rees, M. O. Simonnot, and J. L. Morel, "Short-term effects of biochar on soil heavy metal mobility are controlled by intraparticle diffusion and soil pH increase," *European Journal of Soil Science*, vol. 65, no. 1, pp. 149–161, 2014.
- [33] A. Radenović and J. Malina, "Adsorption ability of carbon black for nickel ions uptake from aqueous solution," *Hemijaska Industrija*, vol. 67, no. 1, pp. 51–58, 2013.
- [34] S. Lagergren, "About the theory of so-called adsorption of soluble substances," *Kungliga Svenska Vetenskapsakademiens Handlingar*, vol. 24, pp. 1–39, 1898.
- [35] Y. S. Ho and G. McKay, "A comparison of chemisorption kinetic models applied to pollutant removal on various sorbents," *Process Safety and Environmental Protection*, vol. 76, no. 4, pp. 332–340, 1998.
- [36] Y.-S. Ho, "Review of second-order models for adsorption systems," *Journal of Hazardous Materials*, vol. 136, no. 3, pp. 681–689, 2006.
- [37] Y. S. Ho and G. McKay, "Pseudo-second order model for sorption processes," *Process Biochemistry*, vol. 34, no. 5, pp. 451–465, 1999.
- [38] J. Cheng, H. Wang, and D. Zhou, "Adsorption-desorption of  $Cu^{2+}$  and  $Cd^{2+}$  on the surface of modified nano-scale black carbon," *Res. Environ. Sci.*, vol. 24, no. 12, pp. 1409–1415, 2011 (Chinese).
- [39] D. Mugisidi, A. Ranaldo, J. W. Soedarsono, and M. Hikam, "Modification of activated carbon using sodium acetate and its regeneration using sodium hydroxide for the adsorption of copper from aqueous solution," *Carbon*, vol. 45, no. 5, pp. 1081–1084, 2007.
- [40] A. Bhatnagar, W. Hogland, M. Marques, and M. Sillanpää, "An overview of the modification methods of activated carbon for its water treatment applications," *Chemical Engineering Journal*, vol. 219, pp. 499–511, 2013.
- [41] T. M. Alslaihi, I. Abustan, M. A. Ahmad, and A. A. Foul, "Microwave irradiated and thermally heated olive stone activated carbon for nickel adsorption from synthetic wastewater: a comparative study," *AIChE Journal*, vol. 60, no. 1, pp. 237–250, 2014.
- [42] L. J. Miles and G. R. Parker, "DTPA soil extractable and plant heavy metal concentrations with soil-added Cd treatments," *Plant and Soil*, vol. 51, no. 1, pp. 59–68, 1979.
- [43] L. Cui, J. Yan, Y. Yang et al., "Influence of biochar on microbial activities of heavy metals contaminated paddy fields," *BioResources*, vol. 8, no. 4, pp. 5536–5548, 2013.
- [44] A. Méndez, A. Gómez, J. Paz-Ferreiro, and G. Gascó, "Effects of sewage sludge biochar on plant metal availability after application to a Mediterranean soil," *Chemosphere*, vol. 89, no. 11, pp. 1354–1359, 2012.
- [45] J. H. Park, G. K. Choppala, N. S. Bolan, J. W. Chung, and T. Chuasavathi, "Biochar reduces the bioavailability and phytotoxicity of heavy metals," *Plant and Soil*, vol. 348, no. 1-2, pp. 439–451, 2011.